Spatially Resolved Quantitative Rheo-optics of Complex Fluids in a Microfluidic Device

Thomas J. Ober,[1] Johannes Soulages,[1] and Gareth H. McKinley[1, a)]

Department of Mechanical Engineering, Massachusetts Institute of Technology, Cambridge, MA 02139, USA

(Dated: 7 May 2011)

In this study, we use micro-particle image velocimetry (μ-PIV) and adapt a commercial birefringence microscopy system for making full-field, quantitative measurements of flow-induced birefringence (FIB) for the purpose of microfluidic, optical-rheometry of two worm-like micellar solutions. In combination with conventional rheometric techniques, we use our microfluidic rheometer to study the properties of a shear-banding solution of cetylpyridinium chloride (CPyCl) with sodium salicylate (NaSal) and a nominally shear thinning system of cetyltrimethylammonium bromide (CTAB) with NaSal across many orders of magnitude of deformation rates ($10^{-2} \leq \dot{\gamma} \leq 10^{4}$ s^{-1}). We use μ-PIV to quantify the local kinematics and use the birefringence microscopy system in order to obtain high-resolution measurements of the changes in molecular orientation in the worm-like fluids under strong deformations in a microchannel. The FIB measurements reveal that the CPyCl system exhibits regions of localized, high optical anisotropy indicative of shear bands near the channel walls, whereas the birefringence in the shear-thinning CTAB system varies more smoothly across the width of the channel as the volumetric flow rate is increased. We compare the experimental results to the predictions of a simple constitutive model, and we document the break-down in the stress optical rule as the characteristic rate of deformation is increased.

[a)] Author to whom correspondence should be addressed: gareth@mit.edu

I. INTRODUCTION

The focus of this study is on the development and refinement of microfluidic-based rheometric techniques for measuring the rheological behavior of complex fluids undergoing high rate or *strong* deformations, for which the viscoelasticity of the material plays an important role in the stress generated in response to an imposed deformation. High rate deformations in complex fluids are commonly achieved even for moderate velocities when the characteristic lengthscale of the flow is small. For example, in the case of the nozzle of an inkjet printer, where the length, $\mathcal{L}$, of the smallest printable feature may be on the order of tens of microns and ejection velocities, v, are on the order of meters per second, characteristic deformation rates, $\dot{\gamma}_c = v/\mathcal{L}$, may easily be on the order of 10^4 s^{-1} or greater.

In this study, the strain rates associated with the flow of micellar solutions in microscale geometries are evaluated with micro-particle image velocity (μ-PIV) measurements using standard equipment. The corresponding stresses associated with the flow are inferred from optically, non-invasive measurements of flow-induced birefringence (FIB) using a commercial birefringence microscopy system (ABRIO$^{\text{TM}}$; CRi, Inc.). The measurements of stress and strain rate may ultimately be coupled to the predictions of select constitutive models to test the performance of those models in predicting the high rate rheology of worm-like micellar solutions.

In the present study we focus on the rheology of worm-like micellar solutions, which are a class of viscoelastic materials that are widely used as rheological modifiers, to tune the viscosity and elasticity of a fluid [Anderson *et al.* (2006); Rehage & Hoffmann (1991)]. Surfactant molecules are composed of both hydrophobic and hydrophilic constituent groups, and as a consequence, under the proper conditions of temperature, salinity and concentration, they associate to form extended, cylindrical molecular aggregates, known as worm-like micelles [Israelachvili (2007)]. The size and shape of the micelles which form in solution significantly influence the rheological properties of the **fluid**. Worm-like micellar solutions are essential constituents of soaps, detergents and shampoos, and are also utilized in inkjet printing, turbulent drag reduction [Rothstein (2008)], and enhanced oil recovery [Kefi *et al.* (2005)]. Here we focus on worm-like micellar systems composed of the surfactant molecules, cetylpyridinium chloride (CPyCl) and cetyltrimethylammonium bromide (CTAB), with the counterion sodium salicylate (NaSal). These compounds are canonical examples that have

been widely used in the rheological literature as model systems for probing the connection between rheological fluid properties and flow characteristics [Cates & Fielding (2006)].

A. Macroscale shear flows and shear-banding

When a semi-dilute and concentrated worm-like micellar system is deformed in a Couette flow, the fluid deforms homogeneously as depicted in Figure 1 (a), provided the average imposed shear rate is sufficiently small, $\dot{\gamma} = U/D \ll \lambda_M^{-1}$, where U is the imposed wall velocity, D is the gap height and λ_M is the characteristic, or Maxwellian relaxation time of the fluid. In this limit, the fluid exhibits a constant zero-shear rate viscosity, η_0, and a first normal stress difference, $N_1 \equiv \tau_{xx} - \tau_{yy}$, that is usually small compared to the applied shear stress, τ_{xy}.

For larger shear rates, $\dot{\gamma} \geq \lambda_M^{-1}$, a shear-thinning viscometric behavior, typically accompanied by the growth of elastic stresses, is generally observed. Indeed, many worm-like micellar solutions exhibit a particularly remarkable shear-thinning behavior, in that over a range of shear rates, $\dot{\gamma}_1 < \dot{\gamma} < \dot{\gamma}_2$, (which can often span multiple orders of magnitude) their effective viscosity may be inversely proportional to shear rate such that an essentially constant shear stress can be applied to deform the material over that range of shear rates. The *stress plateau* is a striking example of the non-linear rheological behavior of worm-like micellar solutions and is discussed in many review articles [Berret (2006); Cates & Fielding (2006); Lerouge & Berret (2010); Olmsted (2008)]. It is generally believed to arise from a non-monotonicity in the underlying flow curve of the material, depicted in Figure 1 (c), resulting in an unstable range of shear rates for which the shear stress associated with homogeneous kinematics decreases with increasing shear rate. In this shear rate regime, it is not possible for a system both to lie simultaneously on a single stable branch of the flow curve and to satisfy the average shear rate, $\dot{\gamma}$. Consequently, the system will partition itself into adjacent layers of material, each undergoing different deformation rates, nominally $\dot{\gamma}_1$ and $\dot{\gamma}_2$ as depicted in Figure 1 (b), yet coexisting at the same applied shear stress, τ_c. This phenomenon is known as *shear-banding* and has formed the basis of many macroscopic rheological studies, as well as theoretical and modeling work by [Fielding (2007); Lu *et al.* (2000); Vasquez *et al.* (2007); Zhou *et al.* (2008)].

In the simplest approximation, the fraction of the gap height, D, occupied by the low

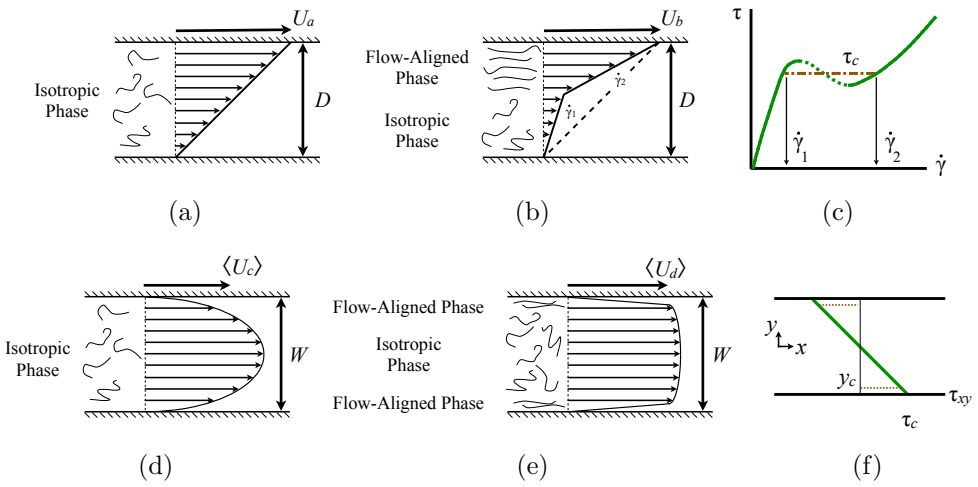

FIG. 1. (a) Homogeneous Couette flow with average shear rate $\dot\gamma_a = U_a/D \ll \dot\gamma_1 \approx \lambda_M^{-1}$, where λ_M is the fluid relaxation time. (b) Inhomogeneous Couette flow for which $\dot\gamma_1 < \dot\gamma_b = U_b/D < \dot\gamma_2$. (c) Non-monotonic underlying flow curve. (d) Homogeneous Poiseuille flow for which the characteristic shear rate $\dot\gamma_c = \langle U_c\rangle/W \ll \dot\gamma_1$, where $\langle U\rangle$ is the average velocity in the channel. (e) Inhomogeneous Poiseuille flow for which, $\dot\gamma_1 < \dot\gamma_d = \langle U_d\rangle/W < \dot\gamma_2$. (f) Shear stress distribution in Poiseuille flow where y_c is the channel position at which $\tau_{xy} = \tau_c$.

shear rate band, β_1, and the high shear rate band, β_2, may be determined by the lever rule such that the average imposed shear rate $\dot\gamma$ is equal to the imposed shear rate, namely

$$\frac{U_b}{D} = \dot\gamma = \beta_1\dot\gamma_1 + \beta_2\dot\gamma_2 \tag{1}$$

where $\beta_1 + \beta_2 = 1$ [Cates & Fielding (2006)]. This lever rule has been observed experimentally for a CPyCl:NaSal:NaCl system [Salmon *et al.* (2003)], but it was found inadequate for describing the shear-banding behavior of other systems [Feindel & Callaghan (2010); Lerouge *et al.* (2008)]. The coexistence of more than two bands is also possible [Miller & Rothstein (2007)]. Evidently, Eq. (1) should be taken only as a simplistic generalization of the complicated shear-banding phenomenon, and much experimental effort aimed at understanding more fully the complex rheological behavior in the shear-banding regime has focused on complementing the rheometry of the bulk flow with detailed measurements of the interplay between flow kinematics and microstructure of the fluid.

In two recent studies of a concentrated CTAB:D_2O system by [Helgeson *et al.* (2009a,b)], measurements of velocity profiles, birefringence and small angle neutron scattering (SANS) in a wall-driven flow were combined to develop a more complete pictures of the microstruc-

tural features of the shear-banding fluid under flow. The authors found that shear-banding in this system was coupled to a flow-induced isotropic-to-nematic transition that could be modeled in terms of an anisotropic drag on the worm-like chains leading to segment-level flow alignment of the micelles. In their study, the nematic phase was found to coincide with the high shear rate band. This result seemed to contradict the earlier findings that the flow-induced nematic phase had a higher viscosity than that of the isotropic phase [Fischer & Callaghan (2000, 2001)]. The difference between shear-thinning and shear-banding worm-like micellar solutions using 2:1 molar CPyCl:NaSal systems of varying concentrations in 0.5 M NaCl has also been investigated [Hu *et al.* (2008)]. Despite considerable experimental effort, a universal explanation for the molecular mechanism behind the shear-banding phenomenon has not yet been realized [Cates & Fielding (2006)].

Velocity profiles of worm-like micelles in Poiseuille flow in macroscale devices have also been observed using nuclear magnetic resonance measurements [Mair & Callaghan (1997)], particle image velocimetry [Méndez-Sánchez *et al.* (2003)] and particle tracking velocimetry [Yamamoto *et al.* (2008)]. As the flow rate through the pipe was increased, a transition from a Newtonian-like velocity profile to a profile with thin regions of high shear rate near the walls and plug-like flow in the core of the fluid was commonly observed. For the flow rates coinciding with the high shear rate bands, a marginal change in wall shear stress led to very large changes in the volumetric flow rate, this phenomenon known in the literature as *spurt* [McLeish & Ball (1986); Renardy (1995)].

Macroscale rheometry alone cannot be used to obtain a complete picture of shear-banding. Hence it is necessary to use microstructural probes (*e.g.* birefringence [Fuller (1990, 1995)]) to measure the molecular anisotropy giving rise to shear-banding and elastic stresses. Additionally, macroscale rheometry is often confounded by the onset of edge fracture, flow instabilities and air entrainment [Fardin *et al.* (2009); Tanner & Keentok (1983); Wheeler *et al.* (1998)], limiting the maximum observable shear rates to values $\dot{\gamma} \leq \dot{\gamma}_2$. Microfluidic devices, however, offer a means of overcoming this limit in observable deformation rates, facilitating investigation of the connection between flow kinematics and microstructual feature of worm-like micellar systems in the non-linear regime.

B. Microscale shear flows

Microfluidic rheometry may be exploited to explore the rheological properties at high deformation rates ($10^2 < \dot{\gamma} < 10^5$ s^{-1}) for many fluids using relatively small sample volumes [Pipe *et al.* (2008); Pipe & McKinley (2009)]. Because of the ease of fabrication, microfluidic shear rheometry typically focuses on straight, high aspect ratio rectangular duct of width, W, height, H and length, L, for which $W \ll H \ll L$. However, more complicated miscroscale geometries have been used to observe both shear and extensional flows [Kang *et al.* (2005, 2006); Oliveira *et al.* (2008); Rodd *et al.* (2005); Soulages *et al.* (2009)]. For rectilinear flows, the shear stress at any position along the width of the channel is known from direct integration of the equation of motion and the corresponding shear rate can be calculated from the local velocity profile which is often measured with micro-particle image velocimetry (μ-PIV). Knowledge of the local shear rate and shear stress can then be used to directly ascertain the flow curve. This process, however, cannot provide information on local elastic stresses, which instead can be measured using rheo-optical probes described below. For shear-thinning or shear-banding micellar solutions in Poiseuille flow, a transition from a Newtonian, parabolic profile at low flow rates depicted in Figure 1 (d), to a banded profile in Figure 1 (e), occurs above a critical wall shear stress [Masselon *et al.* (2008); Nghe *et al.* (2008)], coinciding with Weissenberg number of order unity ($Wi = \lambda_M \langle U \rangle / W \approx 1$).

The microfluidic rheometry of shear-thinning polyethylene oxide solutions has been studied in a rectangular, polydimethylsiloxane (PDMS) microchannel [Degre *et al.* (2006)]. They found good agreement between their measurements of viscosity from the flow in the microchannel and that measured with a conventional Couette rheometer, but noted that a more rigid geometry was needed to test highly viscous fluids. A silica glass geometry was used to study worm-like CPyCl:NaSal:NaCl system by [Guillot *et al.* (2006)], who found good agreement between their viscosity measurements in the microchannel and from the rheometer for all shear rates examined.

An important feature noted in microfluidic studies of complex fluids in rectilinear shear flows has been the role of channel size and aspect ratio. This issue has recently been considered in detail using numerical simulation [Cromer *et al.* (2010); Nghe *et al.* (2010)]. In contrast to flows of simple Newtonian fluids, the confining effects of channel walls of a 1 mm $\times$ 200 μm glass channel were found to give rise to non-local (*i.e.* diffusive) effects that

influence the numerical value of the stress plateau in CPyCl:NaSal:NaCl and CTAB:$NaNO_3$ systems [Masselon *et al.* (2008)]. Experiments with the same CTAB:$NaNO_3$ solution in a 1 mm $\times$ 67 μm glass channel, however, were found not to affect the overall flow curve [Nghe *et al.* (2008)].

To date, the body of scientific literature regarding flows of micellar solutions at the microscale is considerably smaller than that for corresponding macroscale flows. Additionally, very few microfluidic studies have considered anything beyond the kinematics in microfluidic devices offering little insight into the corresponding state of microstructural stress and orientation of the fluid. Microstructural probes, such as spatially resolved measurements of flow-induced birefringence serve to enhance the present understanding of the complex relationship between stress, flow kinematics and the microstructural state of worm-like micellar systems.

C. Flow-induced birefringence

Flow-induced birefringence (FIB) measurements may be used to observe the degree of molecular alignment and stretching in a material and, provided the deformation of the microstructural network is affine, these measurements may be related to the stress in the material through the *stress optical rule* [Fuller (1995); Larson (1998)]. According to this rule, the optical anisotropy, Δn, in a homogeneous, viscoelastic network of Gaussian chains is linearly proportional to its principal stress difference, $\Delta\sigma$, such that $\Delta n = C\Delta\sigma$, where C is the stress optical coefficient and is generally an empirically determined value for a particular material. A list of published values of stress optical coefficients for relevant micellar fluids is given in Table I. The magnitudes of C for worm-like micellar systems are large (typically 10^2 times greater than that of polymer systems) making micellar systems well suited to experimental studies in microfluidic devices. Furthermore, C is found to vary only weakly with temperature, but it does exhibit a slight dependence on concentration.

A number of papers have used FIB measurements to probe the molecular structure of worm-like surfactant systems and to test the validity of the stress optical rule for micellar systems [Decruppe *et al.* (1997); Rehage & Hoffmann (1991); Shikata *et al.* (1994); Wunderlich *et al.* (1987)], and a comprehensive review is available in [Lerouge & Berret (2010)]. Typically, the stress optical rule holds at shear rates below which the onset of

TABLE I. Published values of the stress optical coefficient for micellar systems.

System	$C \times 10^7$ [Pa^{-1}]	Temperature [^oC]	Source
100:60 mM CPyCl:NaSal	-2.3	20	Rehage & Hoffmann (1991)
10-100:50-300 mM CTAB:NaSal	-3.1	25	Shikata *et al.* (1994)
300:100 mM CTAB:KBr	-0.25	30	Humbert & Decruppe (1998)
300:200 mM CTAB:KBr	-0.36	30	Humbert & Decruppe (1998)
300:300 mM CTAB:KBr	-(0.46-0.41)	30-38	Humbert & Decruppe (1998)
300:400 mM CTAB:KBr	-0.62	30	Humbert & Decruppe (1998)
400-600:100 mM CTAB:KBr	-(0.42-0.96)	30	Humbert & Decruppe (1998)
300:1790 mM CTAB:$NaNO_3$	-2.78	30	Lerouge *et al.* (2000)
30:230 mM CTAB:NaSal	-2.77	25	Takahashi *et al.* (2002)
100:51-340 mM CTAC:NaSal	-(2.5-6.1)	25	Decruppe & Ponton (2003)
5.9:1.4 wt% CPyCl:NaSal, 500 mM NaCl	-1.2	23	Hu & Lips (2005)
[CPyCl]:[NaSal]=2, 500 mM NaCl	-1.74	22.1	Raudsepp & Callaghan (2008)

a rate dependent viscosity occurs. However, it often fails at stresses on the order of the stress plateau for the shear-banding fluids, and for stresses near the onset of shear-thinning for the shear-thinning fluids [Decruppe & Ponton (2003)]. In the CTAB:$NaNO_3$ system deviations between the predictions of the stress optical rule and experimental results were attributed to a deviation from Gaussian chain statistics for large deformation rates [Lerouge *et al.* (2000)]. Complex spatiotemporal behavior in FIB has also been observed for shear rates coinciding with the stress plateau, including striations in the birefringence across the gap and the existence of three distinct birefringent bands at higher shear rates [Lerouge *et al.* (2004)]. Point-wise measurements of birefringence of a shear-banding system across the gap width in a Couette cell geometry were obtained by [Lee *et al.* (2005)]. The authors attributed the observed change in sign of the birefringence between the low and high shear rate bands to the existence of two phases, suggesting that a shear-induced phase separation was an underlying cause of the banding behavior.

In the only prior study of birefringence of a worm-like micellar solution flowing in a microchannel, measurements of FIB were coupled with velocimetry measurements to test the stress optical rule for extensional and shear flows in a 100:60 mM CPyCl:NaSal system and a 30:240 mM CTAB:NaSal system [Pathak & Hudson (2006)]. The authors observed

that the stress optical rule failed in extensional flow for deformation rates at which a sharp birefringence band appeared, indicating high or nearly saturated molecular alignment with the flow. It was also found that the stress optical rule failed at a lower critical Weissenberg number in extensional flow than in shear flow.

D. Present study

In the present microfluidic study we combine the established tool of μ-PIV for measuring flow kinematics with a full-field birefringence microscopy system in order to probe the corresponding molecular orientation associated with the flow. We compare and contrast the response of two different entangled micellar fluids, one of which exhibits shear-banding and one which shows shear-thinning. In Section II we first characterize the rheological and rheo-optical properties of the fluids in steady and oscillatory shear flow. After describing the birefringence system, we proceed in Section III to validate the system by comparing measurements performed in microchannels with corresponding macroscale measurements of the stress-optical rule in a conventional rheometer. We then probe the microstructural response of the fluids at increasingly high deformation rates. Finally, we conclude with a discussion of the FIB measurements and the utility of the birefringence microscopy system in observing the microstructual features of flow worm-like micellar solutions. Although our experiments focus on micellar systems, the experimental techniques used here are readily transferable to the study of other transparent, complex fluids.

II. EXPERIMENTAL METHODS

A. Test fluid formulations and rheological properties

Two different worm-like surfactant formulations have been examined in the present experiments. The first solution consists of 100 mM cetylpyridinium chloride (CPyCl) (Alfa Aesar) and 60 mM sodium salicylate (NaSal) (Alfa Aesar) in de-ionized water. A solution with this composition was discussed at length by [Rehage & Hoffmann (1991)]. The second solution consists of 30 mM cetyltrimethylammonium bromide (CTAB) (Sigma Aldrich) and 240 mM NaSal (Alfa Aesar) in de-ionized water. Similar CTAB solutions were studied by [Shikata *et al.* (1994)]. Both of these solutions were also studied in the only previous

microfluidic birefringence study [Pathak & Hudson (2006)].

The solutions were allowed to equilibrate at room temperature, in a dry and unlighted environment for more than one month from the time of their preparation before any experiments were conducted. Both of these micellar solutions possess large stress optical coefficients, C (*cf* Table I), which make them ideal for the birefringence measurements described in detail below. These two systems exhibit distinctly different rheological behavior under shear; they are both strongly shear-thinning, but the CPyCl system exhibits a stress plateau, across many decades of shear rates.

TABLE II. Rheological and rheo-optical properties of the test solutions at 22 °C. ⋆The stress-optical coefficient was measured at 23±1 °C, but previous studies [Humbert & Decruppe (1998)], indicate a weak temperature dependence of C over a temperature range of ±1 °C.

		100:60 mM CPyCl:NaSal	30:240 mM CTAB:NaSal
Maxwell Model	λ_M [s]	2.9	1.7
	η_0 [Pa.s]	82	8.1
	G_0 [Pa]	28	4.7
	$\Psi_{1,0}$ [Pa.s^2]	452	26
Ellis Model	η_0 [Pa.s]	83	8.3
	α	25	2.8
	$\tau_{1/2}$ [Pa]	15	4.1
Additional Parameters	Ψ_1 [Pa.s^2]	3	3
	$^\star C \times 10^7$ [Pa^{-1}]	-1.1	-3.8

1. Linear viscoelasticity

The storage and loss moduli, $G'(\omega)$ and $G''(\omega)$ of both micellar solutions at 22 °C were measured with an AR-G2 stress-controlled rheometer (TA Instruments) using a 40 mm diameter, steel 2° cone-and-plate. The resulting data from the small amplitude oscillatory shear tests have been fitted with the single mode Maxwell model given in Eq. (2), following the method of [Turner & Cates (1991)].

$$G'(\omega) = \frac{G_0(\lambda_M\omega)^2}{1+(\lambda_M\omega)^2} \quad \& \quad G''(\omega) = \frac{G_0\lambda_M\omega}{1+(\lambda_M\omega)^2} \tag{2}$$

From this fit, values of Maxwellian stress relaxation time, λ_M, zero-shear rate viscosity, η_0, and elastic modulus, $G_0 \equiv \eta_0/\lambda_M$, in Table II were determined. Both fluids have Maxwell relaxation times on the order of one second.

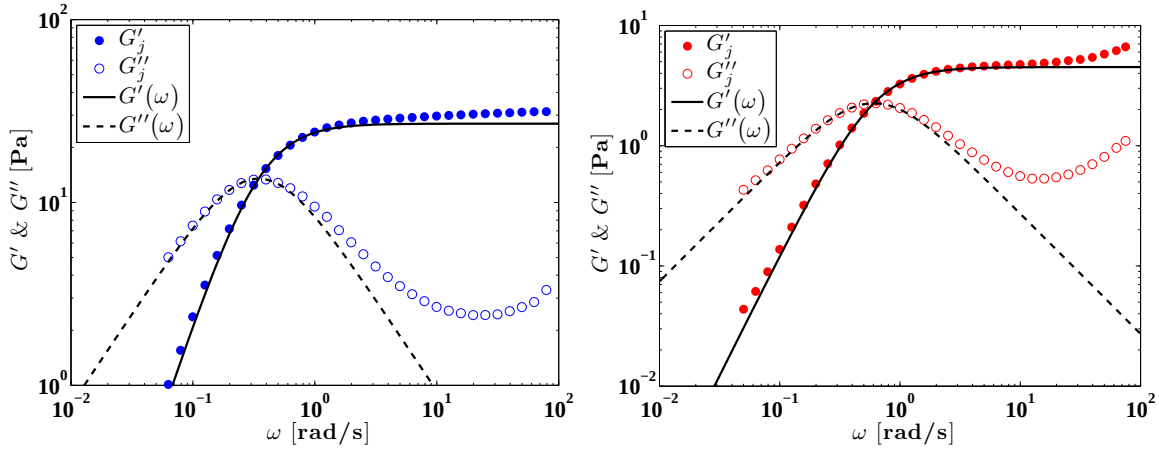

FIG. 2. Storage and loss moduli of 100:60 mM CPyCl:NaSal and 30:240 mM CTAB:NaSal solutions in SAOS at 22 °C. (a) CPyCl:NaSal 100:60 mM. (b) CTAB:NaSal 30:240 mM. The solid and dashed lines are the resultant fit of the low frequency data ($\omega_j \leq \lambda_M^{-1}$) of a single mode Maxwell model with relaxation time, λ_M, and modulus, G_0 given in Table II.

2. Steady shear rheology

The steady shear rheology of these systems at 22 °C and at moderate shear rates ($\dot{\gamma} \leq 10\lambda_M^{-1}$) was measured using a 50 mm diameter, 2° cone-and-plate geometry on an ARES LS-2 strain-controlled rheometer (TA Instruments). Measurements at each shear rate were averaged over a 30 second sampling period following a 120 second delay. The steady shear data is presented in Figure 3, and summarized in Table II. In the limit of low shear rates ($\dot{\gamma} \ll \lambda_M^{-1}$), both fluids exhibit Newtonian behavior. For shear rates of the order $\dot{\gamma} \simeq \lambda_M^{-1}$ or greater, both fluids exhibit shear-thinning, which may be fit empirically with the Ellis model in the form [Bird *et al.* (1987)]:

$$\eta = \frac{\eta_0}{1 + \left(\frac{\tau_{xy}}{\tau_{1/2}}\right)^{\alpha-1}} \tag{3}$$

where η_0 is the zero-shear rate viscosity, $\tau_{1/2}$ is the value of the shear stress at which the

viscosity is equal to half its zero-shear rate value, and α is a fitting coefficient as listed for both fluids in Table II. The Ellis model reduces to the simpler Ostwald Power Law model, $\eta = m\dot{\gamma}^{n-1}$ [Bird *et al.* (1987)], in the limit of $\tau_{xy} \gg \tau_{1/2}$, with $\alpha = n^{-1}$. Fits of this model to the flow curve of each fluid are shown in Figure 3 (b). It is apparent from Figure 3, that for shear rates $\dot{\gamma} \geq \lambda_M^{-1} \approx 0.25$ s^{-1}, the CPyCl exhibits a pronounced stress plateau, $\tau_{plateau} \approx 15$ Pa, suggesting a possible shear-banding behavior [Cates & Fielding (2006); Rothstein (2008)]. In this regime, the large value of α indicates that the viscosity of the CPyCl system is essentially inversely proportional to shear rate. These results for the CPyCl system are very similar to those reported by [Lee *et al.* (2005)]. For the shear rates measured with the ARES, the CTAB system may be seen to exhibit clear shear-thinning, with $\eta \sim \dot{\gamma}^{-0.6}$, for measured shear rates $\dot{\gamma} \geq 0.5$ s^{-1}, but it does not show a constant stress plateau at any point.

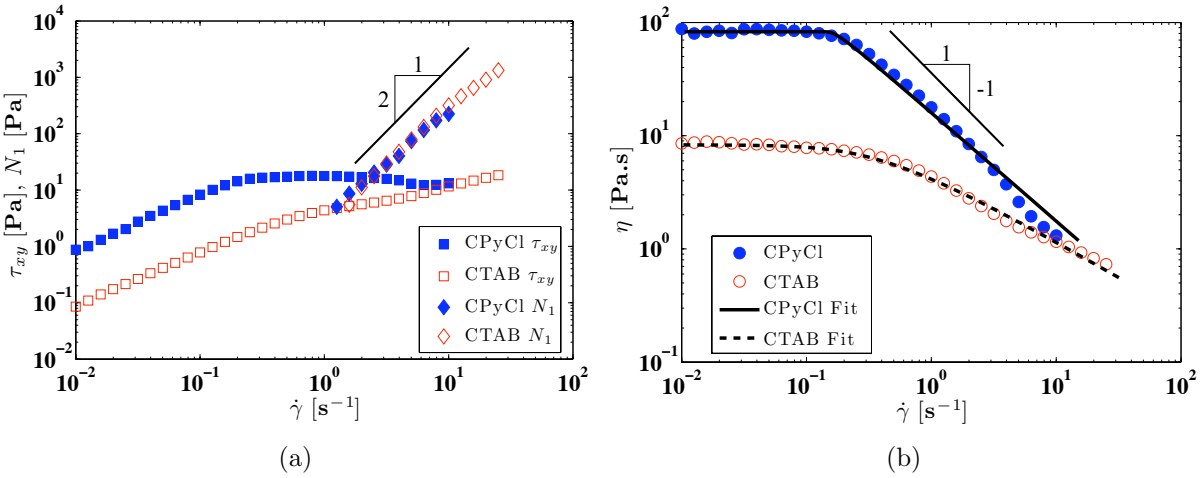

FIG. 3. Steady shear rheology of 100:60 mM CPyCl:NaSal and 30:240 mM CTAB:NaSal solutions at 22 °C. (a) Steady shear stress and first normal stress difference. (b) Steady shear viscosity. The fitted curves are those of the Ellis model with parameters from Table II. The solid black line of slope −1 indicates an inverse proportionality in viscosity with shear rate.

The first normal stress difference can only be measured at shear rates greater than $\dot{\gamma} \approx 3\lambda_M^{-1} \approx 1$ s^{-1}, on account of the lower resolution limit of the normal force transducer (corresponding to about 1 Pa). Both fluids exhibit similar values of first normal stress differences, N_1 over the measurable range. The first normal stress difference for both fluids increases initially quadratically with shear rate, $N_1 \sim \dot{\gamma}^2$, which is depicted by the black line in Figure 3 (a). The quadratic scaling is in agreement with the predictions of the

upper convected Maxwell model, see [Bird *et al.* (1987)], for which the first normal stress coefficient is predicted to be $N_1/\dot{\gamma}^2 = \Psi_{1,0} = 2\eta_0\lambda_M$. This value is, however, a substantial over-estimate of the actual measured first normal stress coefficient, since, for the shear rates at which N_1 was measured, the viscosity of neither fluid is close to the respective zero-shear rate value. In reality, for both systems, $\Psi_1 \approx 3$ Pa.s^2. **We note that the quadratic scaling of N_1 for this shear-banding CPyCl fluid in the shear-banding regime is experimentally repeatable, though it differs from the subquadratic or linear scaling with shear rate observed for other shear-banding fluids, [Helgeson *et al.* (2009b)].** At higher shear rates, $\dot{\gamma} > 10$ s^{-1} for the CPyCl system, and at $\dot{\gamma} > 30$ s^{-1} for the CTAB system, the meniscus of the test fluid becomes unstable and a large fraction of the sample is ejected from the gap. This instability rendered high shear rate rheometry of these fluids with a rotational rheometer impossible, and provided further motivation for pursuing microfluidic rheometry.

3. High shear rate rheology

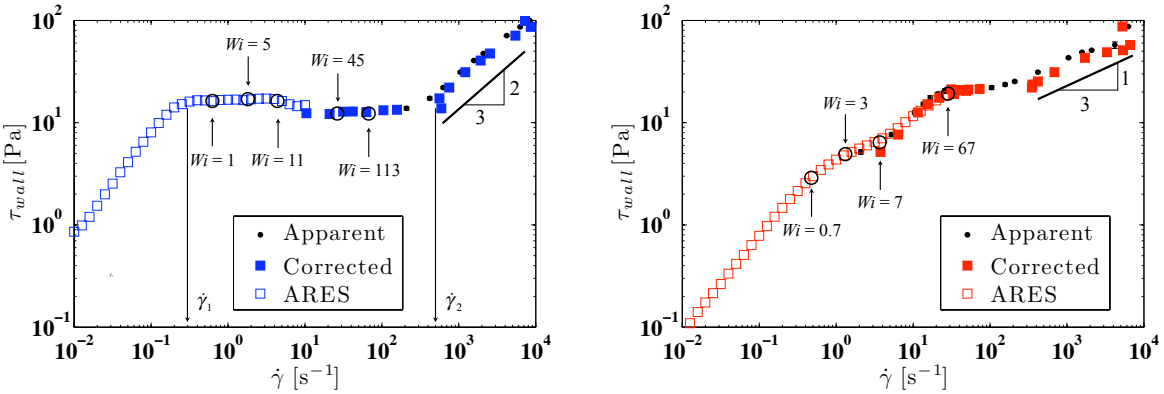

FIG. 4. Steady shear rheology of 100:60 mM CPyCl:NaSal and 30:240 mM CTAB:NaSal solutions at 22-22.5 °C obtained with a microfluidic rheometer (VROC). (a) Shear Stress of 100:60 mM CPyCl:NaSal. (b) Shear Stress of 30:240 mM CTAB:NaSal. Markers denoted "apparent" indicate raw results. Symbols denoted "corrected" markers indicate results obtained with the application of the Weissenberg-Rabinowitsch-Mooney Correction in Eq. (4). Hollow symbols indicate results obtained with the ARES rheometer. The large black circles indicate the Weissenberg numbers, $Wi = \lambda_M\dot{\gamma}_c = \lambda_M\langle U\rangle/W$, corresponding to the flow rates in the microchannel experiments we made. **The solid black lines with indicated slope have been added only to guide the eye.** (a) Symbols $\dot{\gamma}_1$ and $\dot{\gamma}_2$ indicate the limiting shear rates of the stress plateau.

The high shear rate rheology of both solutions was determined with a microfluidic Viscometer/Rheometer-on-a-Chip (VROC, RheoSense Inc.), and the resultant flow curves are presented in Figure 4, up to shear rates of $\dot{\gamma} = 10^4$ s^{-1}. The VROC device is a high aspect ratio, rectangular microfluidic slit rheometer. The channel width, height and length are, respectively, $W = 51.2$ μm, $H = 3.308$ mm and $L = 8.8$ mm; additional details of this system are described in [Pipe *et al.* (2008)]. The channel is fitted with four inline, 800×800 μm^2 MEMS-based pressure transducers along the centerline.

The temperature of the test fluids was controlled with a thermal jacket system (Rheosense Inc.), coupled with an F12-ED Refrigerated/Heating Circulator (Julabo Inc.). Temperature within the channel was recorded with an integrated sensor in the VROC device, and varied between 22 and 22.5 °C throughout the duration of the tests. The pressure drop, ΔP, along the length of the channel was measured for each imposed flow rate and related to the wall shear stress by $\tau_{wall} = \Delta PW/2L$. The Weissenberg-Rabinowitsch-Mooney Correction in Eq. (4) was applied to account for shear-thinning and to determine the true wall shear rate [Pipe *et al.* (2008)], using:

$$\dot{\gamma}_{wall} = \frac{\dot{\gamma}_N}{3}\left(2 + \frac{d\ln\dot{\gamma}_N}{d\ln\tau_{wall}}\right) \tag{4}$$

where $\dot{\gamma}_N = 6Q/HW^2$ is the wall shear rate of a Newtonian fluid corresponding to the volumetric flow rate, Q, in the rectangular channel. Finally, a third order polynomial was fit to five consecutive data points to determine numerically the local differential correction term in Eq. (4) for each data point.

For the CPyCl solution a stress plateau for apparent shear rates $0.2 \leq \dot{\gamma} \leq 500$ s^{-1} can be observed in Figure 4 (a). There is a very clear reduction in the measured value of the stress plateau from $\tau_{plateau,ARES} \approx 15$ Pa as measured on the macroscale, ARES rheometer to $\tau_{plateau,VROC} \approx 12$ Pa as measured with the microfluidic-slit rheometer. This reduction in the value of $\tau_{plateau}$ may possibly be caused by slip or non-viscometric effects in the entrance and exit regions of the channel, but it is also qualitatively in agreement with the predictions of the VCM model for worm-like micelles flowing in rectangular channels, when non-local (stress diffusion) effects on the flow curve are considered [Cromer *et al.* (2010)]. Non-local effects result in the reduction in value of $\tau_{plateau}$ as the slit width of the channel is decreased due to the increasing importance of Brownian motion and the coupling between

stress and microstructure of the micellar system when the length scale of the flow geometry is of the order of the the width of the interface between shear bands [Olmsted (2008)]. This interfacial width, $\ell = \sqrt{\mathcal{D}\lambda_M}$, depends on the relaxation time of the system, λ_M, and the self-diffusion coefficient $\mathcal{D}$. Taking $\mathcal{D} \sim O(10^{-11} - 10^{-9})$ m^2/s [Cromer *et al.* (2010); Helgeson *et al.* (2009b)], we estimate for the CPyCl system in our study, $5 < \ell < 50$ μm, which is of the order of W, the channel width of the VROC, confirming that non-local effects can influence the resultant, high shear rate flow curve in Figure 4 (a). At shear rates greater than approximately $\dot{\gamma}_2 \approx 500$ s^{-1}, the shear stress increases once again with increasing shear rate. In this high shear rate branch of the flow curve, the Reynolds number defined by the rate dependent viscosity, $Re = \rho\langle U\rangle D_h/\eta(\dot{\gamma}_{wall})$, ($\rho = 1100$ kg/m^3, hydraulic diameter $D_h = 2HW/(H+W) \approx 2W = 100$ μm) remains less than unity for all $\dot{\gamma}$ indicating viscous, laminar flow. **For this fluid, the** stress increases sublinearly with shear rate ($\tau \sim \dot{\gamma}^{2/3}$) for $\dot{\gamma} \geq \dot{\gamma}_2$, suggesting that the classical assumption of a high shear rate branch with constant, Newtonian-like viscosity (as for example in the Johnson-Segalman model [Johnson & Segalman (1977)]) is inadequate for describing this fluid. **Nevertheless, the rheology of worm-like micellar fluids in the high shear rate branch is relatively unestablished, and further study of this power-law scaling for $\dot{\gamma} > \dot{\gamma}_2$ is warranted.**

The flow curve of the CTAB solution is presented in Figure 4 (b). At all shear rates measured with VROC, the CTAB system exhibits a continually shear-thinning response, but for a small range of shear rates spanning $30 \leq \dot{\gamma} \leq 100$ s^{-1}, the CTAB solution also exhibits a stress plateau indicative of shear-banding. At shear rates beyond, $\dot{\gamma} > 300$ s^{-1}, the stress increases weakly with increasing shear rate ($\tau \sim \dot{\gamma}^{1/3}$). It is noteworthy that the scaling of stress with shear rate is roughly the same for 0.5 s$^{-1} \leq \dot{\gamma} \leq 30$ s^{-1} and $\dot{\gamma} > 300$ s^{-1}.

B. Flow-induced birefringence

In the present study, we are also interested in determining the material stresses and molecular orientation from measurements of flow-induced birefringence. The stress-optical rule states that the principal stress difference, $\Delta\sigma \equiv \sigma_1 - \sigma_2$, is linearly proportional to the difference between the ordinary and extraordinary indices of refraction, Δn, with stress-optical coefficient, C the proportionality coefficient. This rule is written

$$\Delta n = C\Delta\sigma \tag{5}$$

The principal stresses, σ_1 and σ_2, are the eigenvalues of the two-dimensional stress tensor which characterizes the deviatoric stresses associated with a material deformation, and may be related to the stresses in the xy-frame by

$$\Delta\sigma = \sqrt{N_1^2 + 4\tau_{xy}^2} \tag{6}$$

where τ_{xy} is the shear stress and $N_1 \equiv \tau_{xx} - \tau_{yy}$ is the first normal stress difference.

The second quantity of interest is the azimuthal angle, χ, and corresponds to the orientation of the molecules with respect to the x-axis, the direction of flow in the channel. For the systems studied here, the stress-optical coefficient is negative ($C < 0$) and hence the value of χ indicates the orientation of the fast optical axis of the micelles. The azimuthal angle is related to τ_{xy} and $\Delta\sigma$ by

$$\chi = \frac{1}{2}\sin^{-1}\left(\frac{2\tau_{xy}}{\Delta\sigma}\right) \tag{7}$$

1. Measurements of the stress-optical coefficient

The optical anisotropy cannot be measured directly, but must be inferred from measurements of sample retardance, δ. This quantity may be related to the optical anisotropy of a material, if a constant value for the refractive index difference, Δn can be assumed along the direction of light propagation. In this case, for a birefringent sample having depth, H, along the direction of light propagation, the retardance and optical anisotropy are related by the expression

$$\frac{\delta}{2\pi} = \frac{\Delta n H}{\lambda} \tag{8}$$

where λ is the wavelength of the incident light. Provided this relationship is valid, Eq. (5) and (8) can be combined and separate measurements of birefringence, Δn, and mechanical stress, $\Delta\sigma$, can be combined to determine the stress-optical coefficient, C.

Measurements of flow-induced birefringence were made at an ambient temperature of

23 ± 1^o C, with a Couette cell ($r_1 = 15$ mm, $r_2 = 17$ mm, gap $h = r_2 - r_1 = 2$ mm, optical path length of $H = 20$ mm) using the optical analyzer module (OAM) on the ARES rheometer and the same forward-backward stepped shear rate procedure described in [Helgeson *et al.* (2009b)]. The time-averaged values are shown in Figure 3. Eq. (5) and Eq. (7) may be rearranged to obtain a linear relationship of the stress-optical rule between the quantity, $\frac{1}{2}|\Delta n \sin(2\Theta)|$, and the shear stress, τ_{xy}. In Figure 3 we see this relationship holds for low stresses. The onset of a breakdown in the stress-optical rule coincides with $\dot{\gamma} \approx \lambda_M^{-1}$ for both fluids. On account of the finite spot size of the incident laser ($d_{spot} \approx 1$ mm), measurements at shear rates coinciding with shear-banding, $\dot{\gamma}_1$, may correspond to spatially averaged quantities across the width of the gap. The flow at shear rates $\dot{\gamma} > 2$ s^{-1} in the Couette cell was also prone to foaming and air entrainment leading to further uncertainty in birefringence measurements and therefore optical data at these shear rates have not been included in Figure 5.

The determined values of C are given in Table II. For the CPyCl system, we find $C = -1.1 \times 10^{-7}$ Pa^{-1}, which is very close to the value given by [Hu & Lips (2005)], listed in Table I, for a similar system, but it is a factor of two smaller than the value given in the initial work by [Rehage & Hoffmann (1991)] for the same system studied here. The magnitude of $C = -3.8 \times 10^{-7}$ Pa^{-1}, for the CTAB system is greater by about 20% than the reported value for similar systems given by [Shikata *et al.* (1994)].

C. Experimental setup for microfluidic rheometry

The basic components for each experiment consisted of a microscope, an imaging system, test geometry and fluid, glass syringe (Hamilton Gastight), and a syringe pump, PHD 4000 programmable pump (Harvard Apparatus). Syringes were connected to test geometries using Tygon® microbore tubing (inner diameter 0.508 mm) (Cole Parmer Instrument Co.). In all tests, the length of the tubing was kept to a minimum (10 cm) in order to reduce compliance in the entire system, thereby shortening the duration of experimental transients. Experiments were performed in climate controlled rooms in which the temperature fluctuated between 22-24 °C for the duration of all experiments.

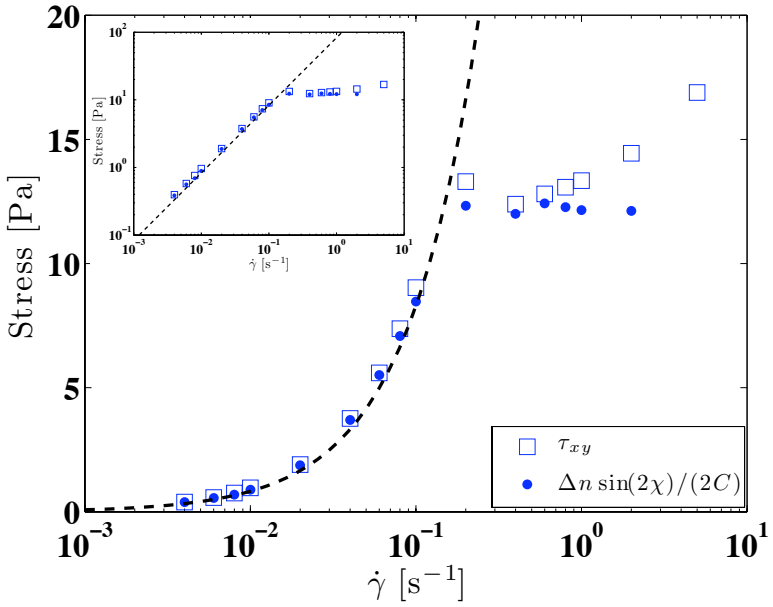

(a)

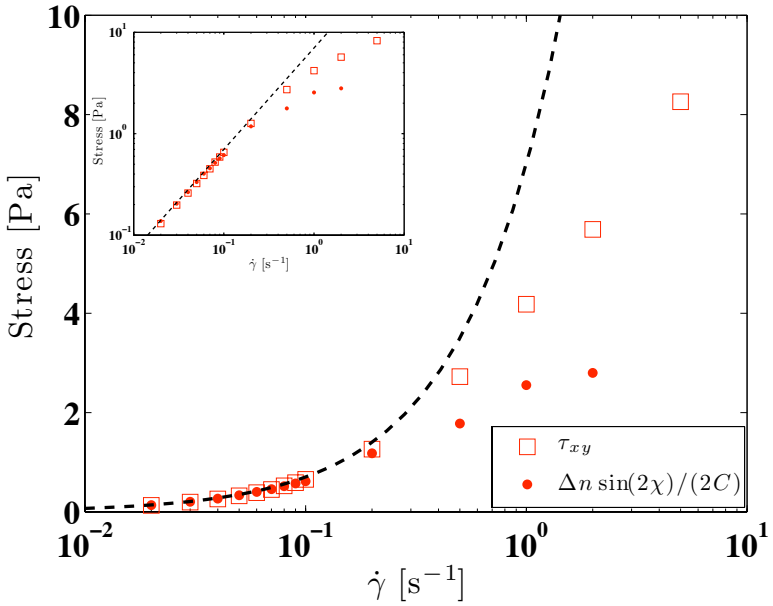

(b)

FIG. 5. Flow-induced birefringence and shear stress against shear rate as measured using the optical analyzer module (OAM) on the ARES rheometer at 23±1 °C: (a) 100:60 mM CPyCl:NaSal system, $C = -1.1 \times 10^{-7}$ Pa^{-1}, (b) 30:240 mM CTAB:NaSal system, $C = -3.8 \times 10^{-7}$ Pa^{-1}. The stress-optical coefficient of each system was determined from the linear portion of the data corresponding to shear rates with constant shear viscosity η_0. The data are plotted semi-logarithmically to accommodate the large range of shear rates. Inset plots on log-log scale. The dashed lines indicate the flow curve given by $\tau_{xy} = \eta_0 \dot{\gamma}$ for each system.

1. *Channel fabrication*

For the microfluidic experiments in the present study, it is necessary to construct a high aspect ratio channel, precluding the use of most lithographic techniques. Therefore, the microchannel was manufactured using a technique similar to that described by [Guillot *et al.* (2006)]. Two anodized, 1 mm × 2 cm × 8 cm aluminum strips were used to construct the sidewalls of the channel as shown in Figure 6. The inside walls of the channel were polished with 2000 grit sandpaper and thoroughly cleaned. A spacer was placed between the two strips to ensure a constant width between the strips, and they were glued together with a two-part epoxy (Devcon). Once the epoxy had set, the spacer was removed and the distance between the strips was checked with an optical microscope in order to ensure that the channel walls were parallel, to within fabrication errors of ± 5 μm. Thin layers of the same epoxy were spread on the top and bottom of the strips and 150 μm thick microscope cover slips were pressed onto the adhesive. Care was taken to ensure that no epoxy seeped into the channel. Luer stub adapter syringe tips were then adhered to the channel at both ends and additional epoxy was added where needed to ensure the channel was sealed. The dimensions of the straight channel used in this study were width, $W = 130 \pm 5$ μm, height, $H = 1,000 \pm 10$ μm, and length, $L = 5$ cm.

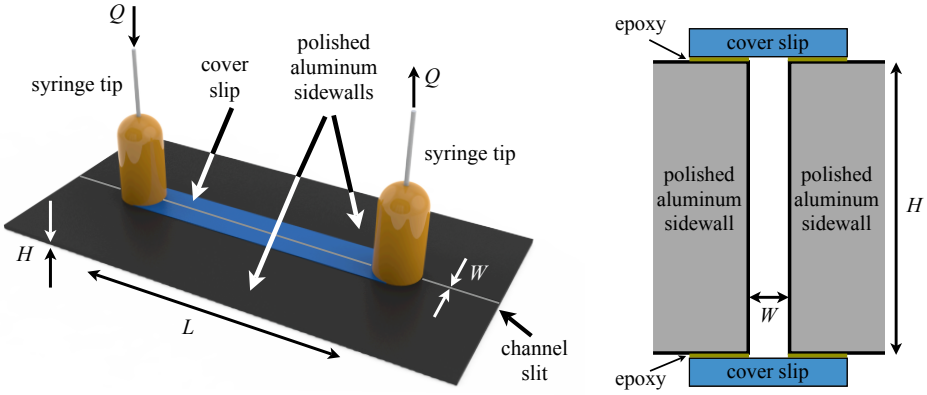

(a) (b)

FIG. 6. (a) Perspective view of straight microchannel. (b) Cross-section of straight channel. Schematic depiction is roughly to scale.

2. *Micro-particle image velocimetry*

Micro-particle image velocimetry (μ-PIV) is a correlative technique, in which one images the temporal displacement of micron sized particulate markers, convecting with a flowing fluid in order to infer the local fluid velocity field [Raffel *et al.* (1998)], as shown in Figure 7. The μ-PIV experiments utilize epifluorescent illumination, whereby the entire volume of a region of flow is illuminated and the spatial resolution of all measurements must be controlled by selecting suitable optical components [Meinhart *et al.* (2000)].

Both test fluids were seeded with 0.02 wt.%, $d_p = 1.1$ μm diameter fluorescent particles (Invitrogen), having excitation and emission wavelengths of 520 and 580 nm, respectively. For neutrally buoyant uncharged particles, the volume fraction of the seed particles may be approximated as $\Phi = 2 \times 10^{-4}$, for which the Einstein correction [Larson (1998)], may be used to predict a minimal increase in viscosity, $\eta = \eta_0(1 + 2.5\Phi + O(\Phi^2)) = 1.0005\eta_0$.

The μ-PIV system used in this study utilizes epifluorescence microscopy and is discussed in detail elsewhere [Rodd *et al.* (2005)]. This system consisted of a 1.4 megapixel (1376 $\times$ 1024 pixels) CCD camera (TSI Instruments, PIV-Cam 14-10) with spacing between pixels, $e = 6.45$ μm, and a double-pulsed 532 nm Nd:YAG laser with pulse width, $\delta t = 5$ ns. A G-2A filter was also used to allow only the emitted light with wavelengths, $\lambda \geq 580$ nm to enter the camera. For a given flow rate, the elapsed time between consecutive image pairs, Δt, ($1.2 < \Delta t < 60,000$ μs), was selected to achieve a particle displacement ($2d_p < \Delta x < 7.5d_p$) suitable for analysis.

Measurements of velocity profiles in the channel were completed with a 10$\times$ 0.25 NA objective. This objective yielded a viewing area encompassing the entire channel width and approximately 1 mm sections along the length (x-axis) of the channel. For the camera and objective used here, the distance over which sample features may be considered in focus is the depth of field, which is $\delta z = 15.8$ μm. The depth of measurement [Meinhart *et al.* (2000)], which is equal to the distance over which additional particles within its vicinity of the focal plane contribute substantially to the overall signal detected by the camera, is $\delta z_m = 47.3$ μm.

At least 35 consecutive images pairs were ensemble-averaged to determine full-field maps of the steady flow velocity profiles using a conventional cross-correlation PIV algorithm (TSI Insight software). Interrogation windows of 16×16 pixels were used in the correlation

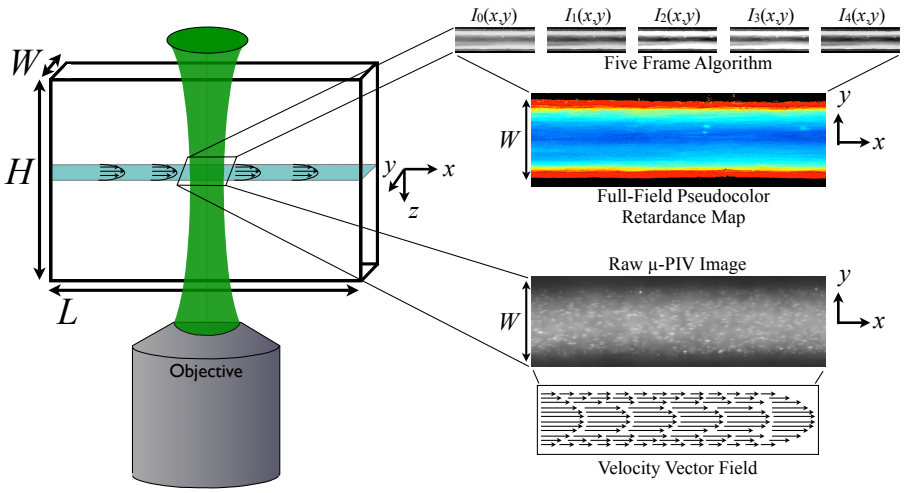

FIG. 7. Schematic depiction of μ-PIV and FIB raw signal measurements on microscope. The xyz-coordinate system is centered along the centroidal axis of the rectangular channel.

scheme, hence the uncertainty in the y-positions of a velocity vector are the width of the interrogation window, corresponding to the error bars parallel to the y-axis shown in velocity profile plots. Each quadrant of an interrogation window was overlapped by the respective quadrant of an adjacent window. Post-processing to remove spurious velocity vectors and any subsequent data analysis of the velocity profiles was completed using MATLAB with a script written by the authors.

A series of measurements were taken at focal planes with a spacing of 50 μm across the channel height. The bottom of the channel was identified as the lowest plane for which a stationary fluorescent particle was in focus. The uncertainty in the vertical position of a focal plane was accordingly the depth of field, δz. Measurement planes more than 450 μm above the bottom of the channel, were found, in general, to capture an insufficient number of particles to determine velocity fields. This weakened signal was attributed to reduced light intensity at higher image planes caused by reflection and absorption of light at lower imaging planes.

The average x-component of the velocity profile at a particular y-position was determined from the ensemble average of all the measured x-velocities in the viewing area at that particular y-position. The error in the value of the x-velocity, therefore, was taken as the standard deviation of the ensemble average, corresponding to the longitudinal error bars in velocity profile plots. The cross-channel, y-components of the velocity profile were found to

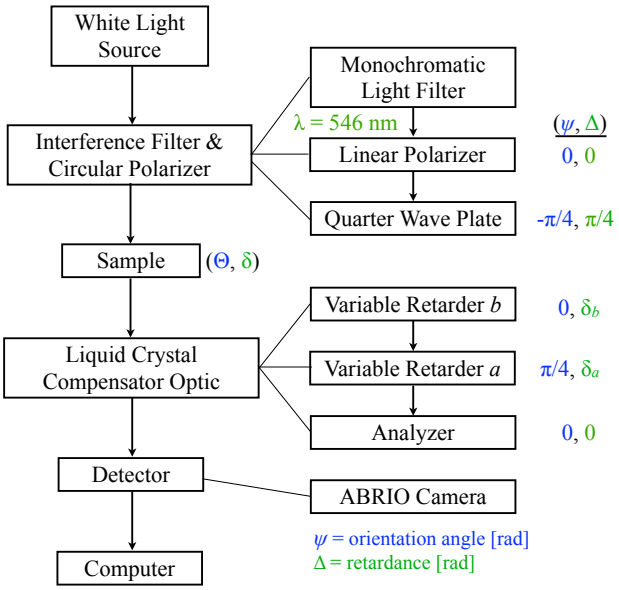

FIG. 8. ABRIO Optical Train.

be negligibly small in comparison to the x-component at any position in the channel.

3. Measurement of birefringence

The ABRIO^{TM} imaging system (CRi, Inc.) is a commercially available instrument originally designed to measure the birefringence of biological samples. The system can measure retardance to within 0.02 nm and yields much higher spatial resolution (pixelsize Δx, $\Delta y \simeq 1$ μm) than can be obtained with the 1 mm spot size of the ARES OAM system. In the present study, the ABRIO system has been adapted in order to measure the birefringence of flowing complex fluids in microscale geometries. The optical train of this device is shown in Figure 8. The basic components of the device are the interference filter and circular polarizer, the liquid crystal compensator optic and the CCD camera.

The white light source, interference filter and circular polarizer together provide a monochromatic ($\lambda = 546$ nm), circularly polarized light wave. The beam then impinges on a birefringent sample and reports both a local retardance, $\delta(x, y)$, and an "orientation angle", $\Theta(x, y)$, which by definition, for the ABRIO system corresponds to the angle between the *slow* optical axis of the sample and the optical axis of the analyzer, (which for our experiments coincides with the x-axis as described below). For the worm-like micellar

systems studied here, the stress-optical coefficient is negative ($C < 0$), and hence the slow optical axis, with angle Θ, is perpendicular to the azimuthal angle, χ, corresponding to the direction of stretching of the molecules. Thus for the systems in this study, we have $\Theta = \chi + \frac{\pi}{2}$, and the azimuthal angle conventionally reported in birefringence studies and orientation angle reported by the ABRIO system are different quantities.

After passing through the sample, the wavefront then passes through a liquid crystal compensator containing two birefringent elements with fixed orientation angles and variable, but known retardances, δ_a and δ_b, and a linear polarizer with a fixed orientation. The emerging beam then impinges on a CCD array detector, which measures the pixelwise intensity of the beam. Provided there is perfect transmittance and no offset of the intensity signal, the ratio of this measured final intensity, $I(x, y)$, and the initial intensity of the beam, $I_{in}(x, y)$ is obtained from Mueller calculus [Fuller (1995)], and is given by the following relationship:

$$\frac{I}{I_{in}} = \frac{1}{2}\left\{1 + \cos(\delta_a)\sin(2\Theta)\sin(\delta) + \cos(\delta)\cos(\delta_b)\sin(\delta_a) - \cos(2\Theta)\sin(\delta)\sin(\delta_a)\sin(\delta_b)\right\} \tag{9}$$

where for compactness, the local spatial variation of each of the quantities δ, Θ and I has not been explicitly indicated.

The operating principles of the ABRIO system is discussed at greater length in [Shribak & Oldenbourg (2003)]. When evaluating a single birefringence image, the ABRIO system records five distinct images, varying the birefringence of the liquid crystal compensator and imposing a swing angle, φ, whose value depends on the prevailing specimen retardance, according to the five frame algorithm listed in Table III. From these five images, a single full-field map of retardance and orientation angle is generated (see Figure 7). The five separate measurements are required to apply the background correction, account for any absorbance of light by the sample or an offset of the intensity signal and to ensure equal sensitivity for all sample orientation angles. The exposure time of each frame depends on the sample birefringence, but it is generally 0.02 to 0.1 seconds.

Once the five intensities have been measured at the specified combinations of δ_a and δ_b given in Table III, Eq. (9) can be simplified and the local values of two intensity ratio parameters, $A(x, y)$ and $B(x, y)$, may be calculated from the following relationships

$$\begin{aligned} A &= \tfrac{I_1 - I_2}{I_1 + I_2 - 2I_0} \tan\left(\tfrac{\varphi}{2}\right) = \sin(2\Theta)\tan(\delta) \\ B &= \tfrac{I_4 - I_3}{I_4 + I_3 - 2I_0} \tan\left(\tfrac{\varphi}{2}\right) = \cos(2\Theta)\tan(\delta) \end{aligned} \tag{10}$$

where again the spatial variation in the intensities, δ, and Θ have not been explicitly indicated. The local values of the retardance, $\delta(x, y)$, and orientation angle, $\Theta(x, y)$, at each point can then be finally calculated from the expressions

$$\delta = \begin{cases} \arctan(\sqrt{A^2 + B^2}) & \text{if } I_1 + I_2 - 2I_0 \geq 0 \\ \pi - \arctan(\sqrt{A^2 + B^2}) & \text{if } I_1 + I_2 - 2I_0 < 0 \end{cases} \tag{11}$$

$$\Theta = \begin{cases} \frac{1}{2}\arctan\left(\frac{A}{B}\right) & \text{for } A \geq 0 \;\&\; B \geq 0 \\ \frac{\pi}{2} + \frac{1}{2}\arctan\left(\frac{A}{B}\right) & \text{for } B < 0 \\ \pi + \frac{1}{2}\arctan\left(\frac{A}{B}\right) & \text{for } A < 0 \;\&\; B \geq 0 \end{cases} \tag{12}$$

TABLE III. Five frame algorithm for the ABRIO system. For each frame, a unique combination of δ_a and δ_b is used, and the corresponding measured intensity is related to the birefringence of the imaged sample by Eq. (9). The set of five measured intensities are then used to determine the parameters A and B given by Eq. (10), which are then used to determine the sample retardance, δ, and orientation angle, Θ, with Eq. (11) and Eq. (12).

Frame Number	δ_a	δ_b	Measured Intensity
0	$\pi/2$	π	I_0
1	$\pi/2 - \varphi$	π	I_1
2	$\pi/2 + \varphi$	π	I_2
3	$\pi/2$	$\pi - \varphi$	I_3
4	$\pi/2$	$\pi + \varphi$	I_4

The ABRIO system can also apply a separate background correction to account for any residual birefringence of the sample. This feature is especially useful for FIB imaging as the optical anisotropy of the fluid sample at rest should be identically zero. The correction is made by recording a user-specified background image, to calculate the reference values of $A_{bg}(x, y)$ and $B_{bg}(x, y)$ from Eq. (10) for the image, and then subtracting the values of $A_{bg}(x, y)$ and $B_{bg}(x, y)$, respectively, from the values of $A_{im}(x, y)$ and $B_{im}(x, y)$ from all subsequent images, to obtain the corrected values of $A(x, y)$ and $B(x, y)$. This correction is

only applicable in the *small retardation limit* [Li & Burghardt (1995)], when the retardance of the sample and background are small compared to the wavelength of incident light [Shribak & Oldenbourg (2003)].

Measurements of FIB in the microchannel were completed with a 20× 0.5 NA objective with the bottom plane of the channel in focus. **In order to minimize possible blurring of the measured birefringence, the angle of the incident cone of light as set by the condenser aperture was 2^o, which was the minimum angle for which the ABRIO system could obtain a strong enough signal to take measurements.** Mean birefringence profiles $\delta(y)$ in the fluid across the channel width were calculated from the full field images $\delta(x, y)$ using the same streamwise averaging employed for the velocity profiles. In order to determine if stress-induced birefringence in the channel itself was significant, glycerine, a non-birefringent Newtonian fluid, was pumped through the channel using the syringe pump at a flow rate of $Q = 300$ μL/hr, corresponding to a relatively high calculated wall shear stress of $\tau_{wall} = 30$ Pa ($\dot{\gamma}_{wall} \approx 30$ s^{-1}). At this wall shear stress no appreciable change in the birefringence ($\delta \leq 3 \times 10^{-3}$ rad) of the channel was observed.

III. RESULTS AND DISCUSSION

A. Dimensional analysis

For steady, two-dimensional flow with volumetric flow rate, Q, in a channel of width, W, and height, H, ($W \ll H$) the average velocity is $\langle U \rangle = Q/WH$. Hence the characteristic deformation rate in the channel is $\dot{\gamma}_c = \langle U \rangle / W$, and the *Weissenberg* number can be defined as

$$Wi = \frac{\lambda_M \langle U \rangle}{W} \tag{13}$$

The experiments reported here correspond to $10^{-1} \leq Wi \leq 10^3$. For $Wi \sim 1$, deformations occur on timescales roughly equal to the relaxation time of the fluid and the onset of non-Newtonian behavior is to be expected. As the magnitude of the Weissenberg number is increased, strong departures from Newtonian behavior are observed, including shear-thinning and considerable optical anisotropy.

The *Deborah* number is defined as the ratio of the fluid relaxation time to a characteristic

timescale for the flow [Dealy (2010)]; which here can be considered to be the residence time of the fluid in the channel for a particular observation distance,

$$De = \frac{\lambda_M \langle U \rangle}{L_{obs}} \tag{14}$$

where L_{obs} is the distance downstream of channel entrance, at which the flow is observed. The magnitude of the Deborah number gives an indication for how fully-developed the flow is expected to be at the point of observation. For $De \ll 1$, the residence time is sufficiently long for viscoelastic memory effects to have decayed. In our microchannel experiments, $10^{-3} \leq De \leq 10$.

The relative importance of inertia and viscosity is characterized by the *Reynolds* number

$$Re_0 = \frac{\rho \langle U \rangle D_h}{\eta_0} \tag{15}$$

where the hydraulic diameter is $D_h = 2HW/(H+W) \approx 2W = 260$ μm for this channel. For the range of flow rates observed in this study, (10 μL/hr $\leq Q \leq 10^4$ μL/hr), the Reynolds number is $10^{-8} \leq Re_0 \leq 10^{-3}$, indicating that inertial turbulence is never a possibility. If the strong rate dependence of the characteristic viscosity of micellar fluids (*i.e.* $\eta(\dot{\gamma}_c)$) is accounted for, using the flow curves measured with VROC in Figure 4, then values of $Re(\dot{\gamma}_c)$ are higher, but never exceed unity, which is again far from the critical Reynolds number required for the onset of turbulence ($Re_c \approx 2000$). **The values of Re_0 obtained can also be used in the correlation for determining the entrance length for a Newtonian fluid, $L_e/D_h = [(0.631)^{1.6} + (0.0442 Re_0)^{1.6}]^{1/1.6}$ [Durst *et al.* (2005)]. According to this correlation, for $Re_0 \ll 1$, $L_e \approx 0.631 D_h \ll L_{obs}$, thus arguments based on viscous Newtonian fluid mechanics would indicate the flow is kinematically fully-developed. The effect of shear-thinning on the entrance length has also been investigated by [Poole & Ridley (2007)], who determined that the entrance length increases at most by 40% beyond the Newtonian result in the creeping flow limit.** As we show in Appendix A, however, viscoelasticity complicates this picture.

An additional dimensionless ratio is the elasticity number, which compares the magnitude of elastic stresses to inertial effects in the flow,

$$El_0 = \frac{Wi}{Re_0} = \frac{\lambda_M \eta_0}{\rho W D_h} = \frac{\Psi_{1,0}\dot{\gamma}_c^2}{\rho \langle U \rangle^2} \tag{16}$$

This parameter is independent of the kinematics of the flow, since it depends only on the properties of the fluid and dimensions of the channel. For the present tests the values given in Table II indicate that $El_0^{CPyCl} = 7.0 \times 10^7$ and $El_0^{CTAB} = 2.4 \times 10^6$. Alternatively, one could define a rate dependent elasticity number using the measured first normal difference $El(\dot{\gamma}_c) = N_1(\dot{\gamma}_c)/\rho\langle U \rangle^2 = \Psi_1/\rho W^2 = 1.6 \times 10^5$ for both the CPyCl and CTAB systems. These large values of the elasticity number are unique to flows in microchannels, and they indicate that inertial effects are negligible compared to elastic stresses. Microfluidic rheometry thus enables measurements of the rheological behavior of complex fluids at high shear rates in the absence of inertial complications.

B. Flow kinematics

Velocity profiles were measured at successive positions, $(-0.5 \leq \frac{z}{H} \leq 0.5)$ across the height of the channel at a fixed observation point downstream **($L_{obs} = 3.5$ cm, $L_{obs}/D_h = 134$)**. Within statistical uncertainty, flow profiles were observed to be invariant along the z-axis for heights corresponding to $|\frac{z}{H}| \leq 0.4$. Profiles measured between approximately 200 and 300 μm above the bottom of the channel ($0.2 \leq \frac{z}{H} \leq 0.3$) are reported as the characteristic two-dimensional velocity profile for a given Wi, similar to the approach of [Nghe *et al.* (2008)]. **To verify this assumption of the characteristic velocity profile, the reported profiles were numerically integrated across the channel width to determine the average measured plug-velocity $U_p = \frac{1}{W}\sum_i u_{x,i}\Delta y$ at that value of $\frac{z}{H}$ to be compared against the imposed nominal velocity $\langle U \rangle$. For all profiles, $U_p/\langle U \rangle \leq 1.15$, revealing that wall effects due to the finite aspect ratio of the channel effectively reduced the channel cross section by less than 15%, with three-dimensional effects thus confined to $|\frac{z}{H}| \geq 0.4$.**

Velocity profiles for the CPyCl solution are shown in both dimensional and scaled dimensionless form in Figure 9 for $1 \leq Wi \leq 45$. The profiles appear to extend beyond the channel width, on account of some variability in the width of the channel (± 5 μm) and the finite spatial error in the velocimetry measurements (5 μm). The most general feature in these profiles is the transition from a mixed Newtonian and shear-banding profile at low

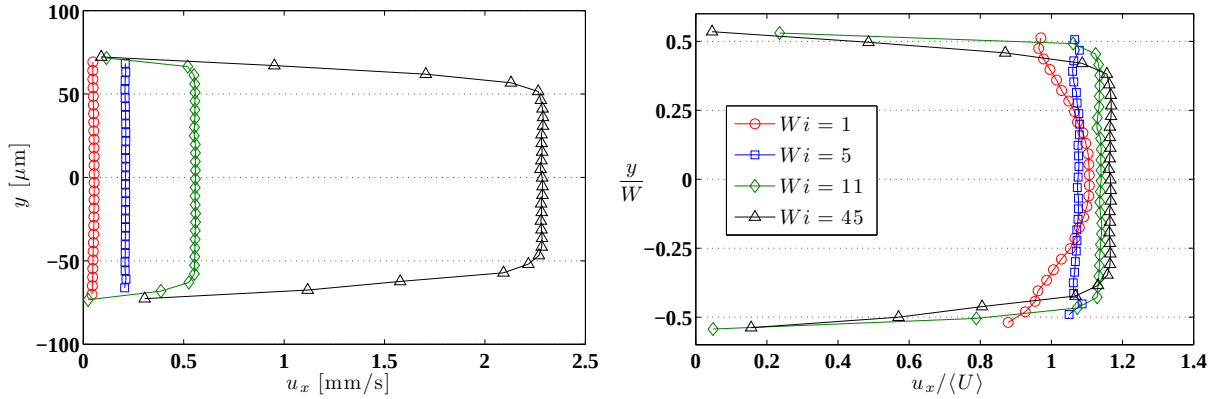

FIG. 9. Representative dimensional (a) and non-dimensionalized (b) velocity profiles for 100:60 mM CPyCl:NaSal at different Weissenberg numbers in the rectangular duct taken at $0.2 \leq \frac{z}{H} \leq 0.3$ above the bottom of the channel at $L_{obs} = 3.5$ cm ($L_{obs}/D_h = 134$).

$Wi \approx 1$ to a very markedly shear-banding, nearly perfect plug-like profile, with $u_{x,max} = \langle U \rangle$ at moderate Wi. At higher $Wi > 10$ a departure from perfect plug-like flow is observed, with $u_{x,max} > \langle U \rangle$, and a progressive increase in the thickness of the shear-banding layer with Wi.

An additional noteworthy feature in the velocity profiles of the CPyCl system, especially at low $Wi \leq 5$ is what appears to be evidence of wall slip between the fluid and the channel walls. At the lowest flow rate this apparent slip may be an artifact of very thin shear-banding layers near the walls, which were too thin to be resolved by the μ-PIV system. The expected thickness of the shear-banding layers can be estimated by assuming the previously described, classical picture of a shear-banding fluid, whereby the shear rate within the band is assumed to be $\dot{\gamma}_2 \approx 500$ s^{-1} which lies at the right hand end of the stress plateau for the CPyCl system presented in Figure 4 (a). To first order, this thickness of the shear-banding layer is $l_{SB} \approx \langle U \rangle / \dot{\gamma}_2$. For $Wi = 1$, the average velocity is $\langle U \rangle = 47$ μm/s and hence $l_{SB} \approx 0.1$ μm. At $Wi = 5$, $\langle U \rangle = 180$ μm/s, the thickness only increases to $l_{SB} \approx 0.4$ μm. For the μ-PIV system used for these experiments, the minimum resolvable feature $e/M = 0.65$ μm and accordingly the shear-banding layer is too thin to be resolved by μ-PIV at low Wi.

Dimensional and dimensionless velocity profiles of the CTAB solution are shown in Figure 10. The CTAB solution exhibits a very clear transition from a parabolic-like velocity profile associated with the flow of a Newtonian fluid at low $Wi \leq 1$, to a flatter U-shaped

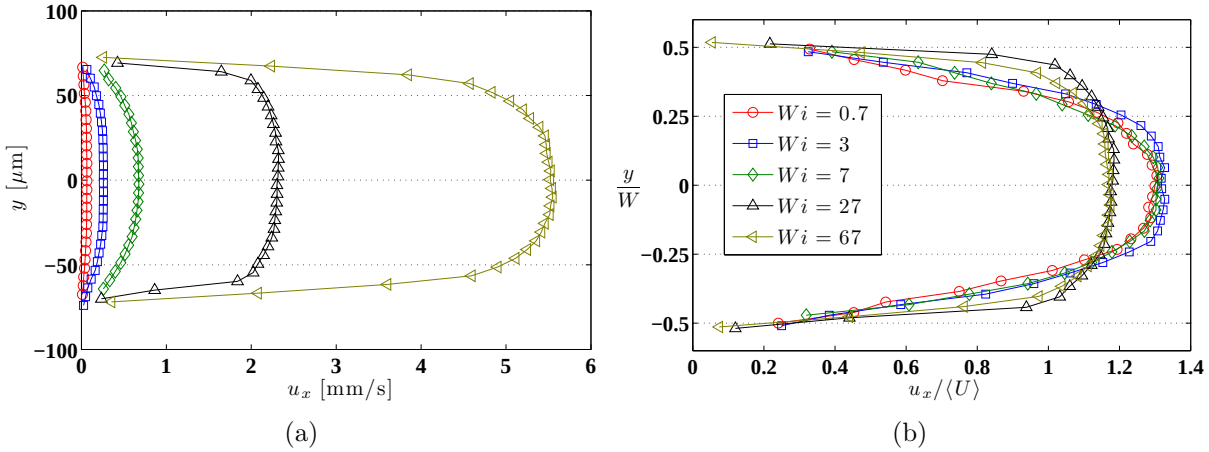

FIG. 10. Representative dimensional (a) and non-dimensionalized (b) velocity profiles for 30:240 mM CTAB:NaSal at different Wi in the rectangular duct taken at $0.2 \leq \frac{z}{H} \leq 0.3$ above the bottom of the channel at $L_{obs} = 3.5$ cm ($L_{obs}/D_h = 134$).

velocity profile characteristic of the flow of a moderately shear-thinning fluid at moderate to high Weissenberg number ($Wi \gg 1$). To within experimental uncertainty (error bars not shown in Figure 10), measured fluid velocities within 5 μm of the wall are equal to or less than about 15% of the maximum velocity in the channel, $u_{wall} \leq 0.15 u_{max}$. Accordingly, wall slip is not a significant contribution to the flow profile at any flow rate.

C. Birefringence and stress

1. *Evolution of the birefringence profiles*

As the fluids flow down the length of the channel, the local deformation rate and therefore the optical anisotropy varies along both the channel width and length, such that we expect $\dot{\gamma}(x, y)$, $\delta(x, y)$ and $\Theta(x, y)$. In order to observe the evolution of the optical anisotropy in the channel, full-field pseudocolor retardance maps, for which the imaged channel area was $(\Delta x_{im}, \Delta y_{im}) = (700\ \mu\text{m}, 130\ \mu\text{m})$, were obtained at $L_{obs} = 1.5$, 2, 2.5, 3, 3.5 and 4 cm **(L_{obs}/D_h = 58, 77, 96, 115, 134, 154)** downstream from the inlet of the channel. Since $\Delta x_{im} \ll L$, and variations in δ are typically small in the x-direction within the field of view Δx_{im}, the local quantity $\delta(x, y)$ can be averaged over the flow direction for each image, to obtain the averaged one-dimensional profiles of $\delta(y)$ shown in Figure 11. For these measurements, a background image was taken without the channel in view, in order

to apply the background correction for the residual birefringence of the optical train only. This approach facilitated observation of the flow-induced birefringence at different positions along the length of the channel without biasing the background correction at all channel positions with that of a single, particular location in the channel. Accordingly, any residual birefringence of the channel, though small compared to the FIB of the flowing fluid, is not accounted for in these images.

For a particular value of Wi, the Deborah number, De, is the dimensionless quantity that dictates how fully-developed one can expect the viscoelastic flow and the optical anisotropy to have become [Dealy (2010)]. For $Wi \leq 75$, the Deborah numbers corresponding to the different L_{obs} listed above are all less than unity, and the retardance profiles were observed to reach a fully-developed profile within the channel length. The spatially fully-developed nature of the flow is revealed by the superposition of retardance profiles with decreasing De shown in Figure 11. For $Wi > 75$, the higher velocities result in Deborah numbers (corresponding to the different observation positions L_{obs}) of order unity or greater indicating that within the length of the channel a fully-relaxed stress profile could not be obtained. Thus spatially-developing FIB profiles were observed through the entire length of the channel.

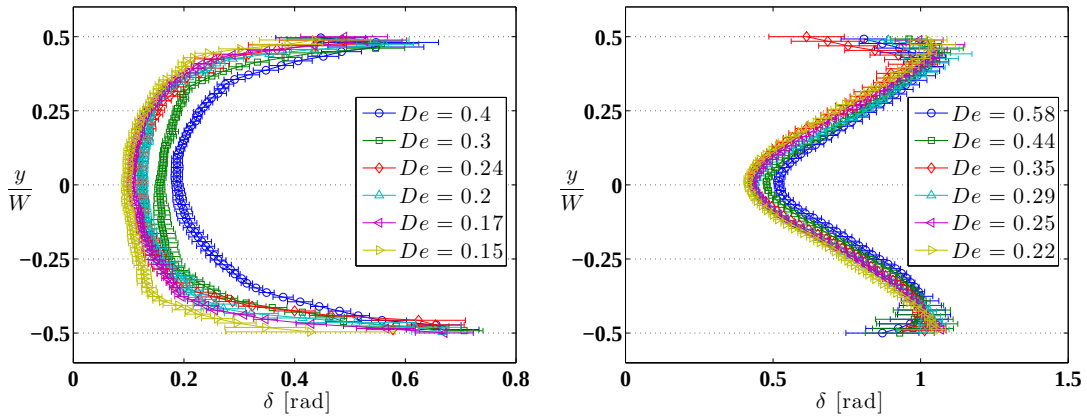

FIG. 11. Retardance profiles at different Deborah numbers, De, (corresponding to different L_{obs}) in the rectangular duct. Error bars correspond to the standard deviation of the retardance values. (a) 100:60 mM CPyCl:NaSal. $Wi = 45$, $Q = 1,000$ μL/hr. (b) 30:240 mM CTAB:NaSal. $Wi = 67$, $Q = 2,500$ μL/hr.

2. *Background corrected birefringence profiles*

Measurements of retardance, $\delta(x, y)$, and azimuthal angle, $\chi(x, y)$, for which the residual birefringence of the channel was corrected, were taken at $L_{obs}/D_h = 134$. Full-field pseudo-color plots of CPyCl retardance, are presented in Figure 12. For fully-developed flow, the quantities $\delta(x, y)$ and $\chi(x, y)$ can be averaged in x, to obtain the steady profiles of $\delta(y)$ and $\chi(y)$ at a selection of Wi, for which $De < 1$, shown in Figures 13.

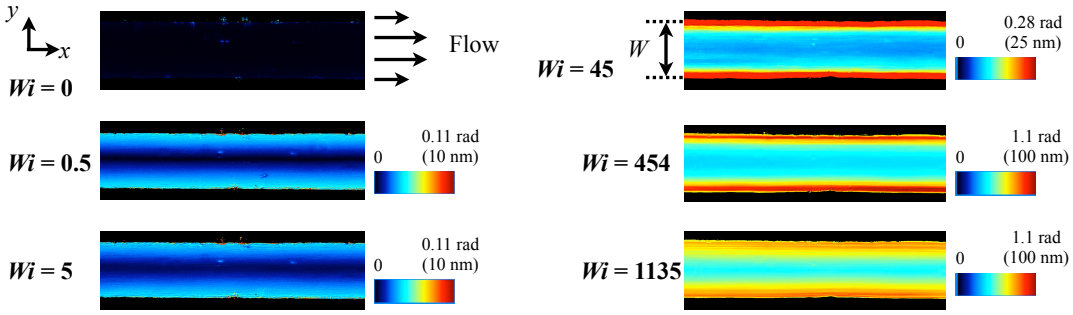

FIG. 12. Pseudocolor plots of retardance maps for the 100:60 mM CPyCl:NaSal solution in the rectangular duct at $L_{obs} = 3.5$ cm ($L_{obs}/D_h = 134$). Color bar indicates linear scaling in retardance for each image. Areas beyond the channel width are shown by the black bands.

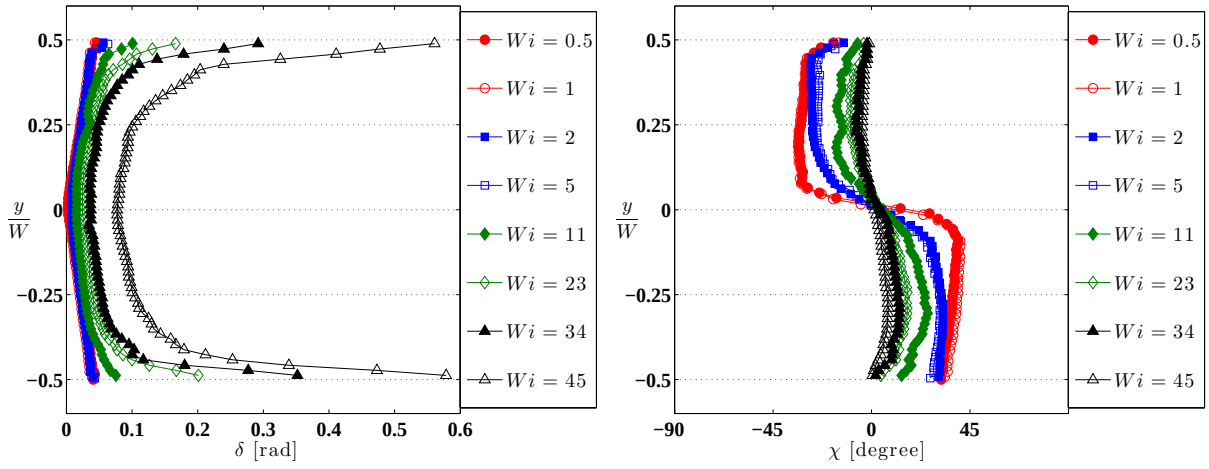

FIG. 13. Experimental retardance and azimuthal angle profiles at increasing Wi for the 100:60 mM CPyCl:NaSal solution in the rectangular duct at $L_{obs} = 3.5$ cm ($L_{obs}/D_h = 134$). (a) Retardance Profiles. (b) Azimuthal Angle Profiles.

At low $Wi < 5$, the retardance profiles increase linearly from the centerline of the channel to the wall, taking on a characteristic V-shaped profile. Since τ_{xy} varies linearly across the channel for rectilinear pressure-driven flow, the linear variation in δ indicates that the shear stress, τ_{xy}, is the predominant contribution to $\Delta\sigma$, given by Eq. (6). The contributions from the normal stress difference, N_1, are confined to a thin region near the wall and are negligibly small for low Wi. For increasing $Wi > 10$, regions of high, but localized, retardance develop near the walls yielding a U-shaped profile, indicating the growth in the thickness of high shear rate bands. The change in retardance at the middle of the channel with increasing Wi is much more gradual when compared to the rapid change in the high shear rate regions near the walls. At higher Wi, however, the retardance along the channel centerline is finite indicating non-zero normal stress difference along the center of the channel. The increased contribution of elastic stresses even in regions of low shear rate near the channel centerline can be rationalized by the possibility of diffusion of elastic stresses due to the importance of non-local effects that have been documented in the microfluidic flows of other complex fluids [Masselon *et al.* (2008)], and recently studied numerically [Cromer *et al.* (2010)].

The azimuthal angle profiles exhibit odd symmetry about the centerline of the channel. At low Wi, the azimuthal angle is $\chi = -45^o$ $(\frac{\pi}{4})$ and $\chi = 45^o$ $(\frac{3\pi}{4})$ on opposite sides of the channel width. These limiting values for χ predicted by Eq. (7) also confirm that τ_{xy} is considerably greater than N_1 for this flow rate, with the change from -45^o to 45^o arising from the change in sign of τ_{xy} on opposite sides of the channel. With increasing Wi, the azimuthal angle approaches 0^o at all points in the channel, further confirming the presence of elastic stresses and high molecular alignment in the direction of flow along the channel centerline.

Background corrected measurements of the flow-induced birefringence in the CTAB system were also taken at $L_{obs}/D_h = 134$. Pseudocolor plots of retardance are shown in Figure 14 and the resultant spatially-averaged retardance and azimuthal angle profiles are presented in Figures 15. For all Weissenberg numbers, retardance profiles take on a consistently V-like shape, indicating that there are no banded regions of localized, high shear rate and normal stresses that cause high, localized retardance near the walls. As seen in the CPyCl system, at higher flow rates for the CTAB system, the retardance along the channel centerline is finite, and the retardance profiles increase monotonically from the centerline to the wall for all Wi. For the sake of visual clarity, however, error bars have not been

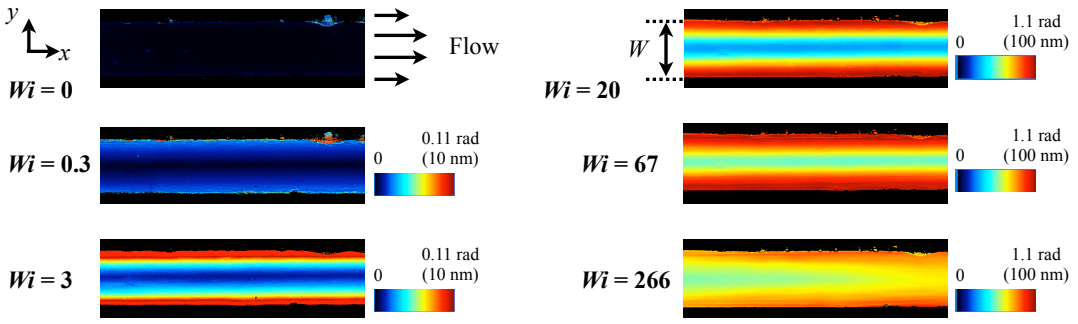

FIG. 14. Pseudocolor plots of retardance maps for the 30:240 mM CTAB:NaSal solution in the rectangular duct at $L_{obs} = 3.5$ cm ($L_{obs}/D_h = 134$). Color bar indicates linear scaling in retardance for each image. Areas beyond the channel width are shown by the black bands.

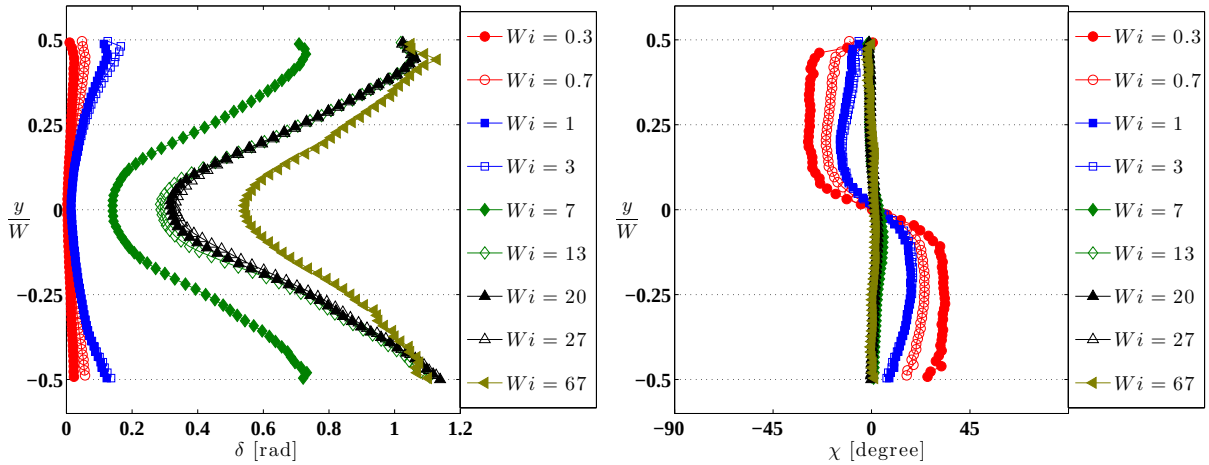

(a) (b)

FIG. 15. Experimental retardance and azimuthal angle profiles at increasing Wi for the 30:240 mM CTAB:NaSal solution in the rectangular duct at $L_{obs} = 3.5$ cm ($L_{obs}/D_h = 134$). (a) Retardance Profiles. (b) Azimuthal Angle Profiles.

shown in Figure 15. **Interestingly, the retardance at the wall exhibits an irregular relationship with increasing flow rate and saturates as the Weissenberg number is increased**.

Anti-symmetry in the azimuthal angle profiles about the channel centerline may also be seen for this system. However, even for the lowest Wi examined here seen in Figure 15 (b), the azimuthal angle did not attain the limiting values of $\chi = \pm 45^o$, indicating that the elastic stresses were substantial enough to partially align the molecules in the flow direction

at all positions across the width of the channel. For high Wi, the azimuthal angle again approaches 0^o across the entire channel, indicating high molecular alignment in the flow direction.

D. Comparison of measurements with theoretical predictions

In order to validate the birefringence microscopy system for use in optical rheometry, we assume the validity of the stress-optical rule and compare the predictions of the Ellis model [Bird *et al.* (1987)], for pressure-driven rectilinear flow to our independent measurements of flow kinematics and FIB. **Although this model is only a generalized Newtonian fluid model, it has been selected here because it can capture both the zero-shear viscosity and rate dependent regime of the fluid and can be used to obtain an analytical result for the velocity profile in the channel given in Eq. 19.** For fully-developed, inertialess flow along the x-axis of the channel with $W \ll H \ll L$ (here $H/W \approx 8$), the governing equation of motion is

$$\frac{\partial P}{\partial x} = \frac{\partial \tau_{xy}}{\partial y} \tag{17}$$

where τ_{xy} is the shear stress and P is mechanical pressure. This equation may be integrated directly with the boundary condition $y = \pm\frac{W}{2}$, $\tau_{xy} = \mp\tau_{wall}$, to obtain $\tau_{xy}(y) = -\tau_{wall}\frac{2y}{W}$, where $\tau_{wall} = -\frac{W}{2}\frac{\partial P}{\partial x}$. Eq. (3) may be multiplied by the shear rate, $\dot{\gamma}$, and with suitable rearrangement, one may obtain the following relation between the velocity gradient and shear stress.

$$\frac{du_x}{dy} \equiv \dot{\gamma} = \frac{\tau_{xy}}{\eta_0}\left[1 + \left(\frac{\tau_{xy}}{\tau_{1/2}}\right)^{\alpha-1}\right] \tag{18}$$

Substitution for $\tau_{xy}(y)$ in Eq. (18), integration and application of the no slip boundary condition $u_x = 0$ at $y = \frac{W}{2}$ yields the resultant velocity profile:

$$u_x = \frac{\tau_{wall}}{4\eta_0}W\left[\left(1 - \frac{4y^2}{W^2}\right) + \frac{2}{\alpha+1}\left(\frac{\tau_{wall}}{\tau_{1/2}}\right)^{\alpha-1}\left(1 - \left|\frac{2y}{W}\right|^{\alpha+1}\right)\right] \tag{19}$$

The average velocity is

$$\frac{1}{W}\int_{-W/2}^{W/2} u_x dy = \langle U \rangle \equiv \frac{Q}{WH} = \frac{\tau_{wall}}{6\eta_0} W \left[1 + \frac{3}{\alpha+2}\left(\frac{\tau_{wall}}{\tau_{1/2}}\right)^{\alpha-1} \right] \tag{20}$$

In the limiting case of $\alpha = 1$, Eq. (19) and (20) reduce to the standard result for a Newtonian fluid with viscosity $\mu = \frac{1}{2}\eta_0$, where the factor of $\frac{1}{2}$ results from Eq. (3). **Since the flow rate, Q, is prescribed in the present study, the wall shear stress τ_{wall} must be determined implicitly from Eq. (20) in order to determine the velocity profile for a given Q.** In this manner, the predicted velocity profiles shown in Figures 16, 17 and 18 were obtained for comparison with the experimentally measured results.

For fully-developed viscous flow of any fluid in a high aspect ratio duct, the shear stress varies linearly with position between $-\tau_{wall} \leq \tau_{xy} \leq \tau_{wall}$, and it is therefore necessarily zero at the centerline of the channel. For a given volumetric flow rate, Q, the shear stress at all positions across the width of the channel can be determined, once τ_{wall} is calculated from Eq. (20). **In this way, the Ellis model was used to predict the shear stress profile, while** the distribution of the **first normal** stress difference across the channel was predicted by interpolation of rotational rheometer data for $N_1(\dot{\gamma})$, as calculated from the spatial gradient of $\dot{\gamma}(y) = \partial u_x/\partial y$ in Eq. (19). When the imposed flow rate is so high that the resulting calculated shear rate at a particular y-position across the channel is higher than the shear rates for which data from the rotational rheometer could be obtained, we cease to provide comparative data. The calculated values of deviatoric stresses, $\tau_{xy}(y)$ and $N_1(y)$, were then used to calculate the principal stress difference, $\Delta\sigma(y)$ from Eq. (6). This value can then be used to predict the expected optical anisotropy, $\Delta n(y)$, from the stress-optical rule in Eq. (5). Finally, the optical anisotropy can be related to the measured retardance, $\delta(y)$, using the assumption that variations in the flow along the height of the channel are negligible so that Δn is invariant along the the z-axis. The anticipated azimuthal angle, which indicates molecular orientation, was calculated from Eq. (7). For the results presented here, $\chi = 0^o$ coincides with the direction of flow (x-axis), with χ increasing counterclockwise, such that $\chi = 90^o$ coincides with the y-axis.

At very high flow rates, the flow is not spatially fully-developed and exhibits streamwise variations as can be seen, for example, in the axial variations in retardance for $Wi = 266$ in Figure 14. Therefore, we limit our quantitative analysis to $Wi \leq 67$ and $De < 1$ where the flow is fully-developed and steady (see Appendix A for additional discussion). A comparison

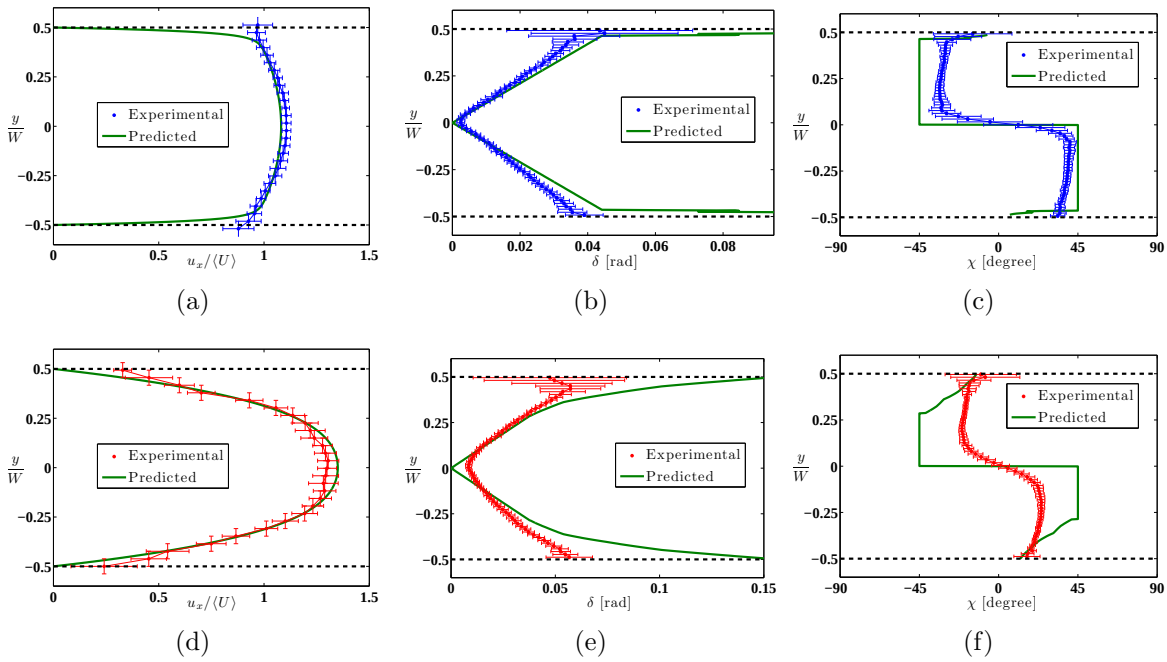

FIG. 16. Representative experimentally-measured and theoretically-predicted velocity, retardance and azimuthal angle profiles at low Wi in the rectangular duct . Data are taken at 200 to 300 μm above the bottom of the channel at $L_{obs}/D_h = 134$. (a)-(c) 100:60 mM CPyCl:NaSal (blue profiles), $Wi = 1$, $Q = 25$ μL/hr. (d)-(f) 30:240 mM CTAB:NaSal (red profiles), $Wi = 0.7$, $Q = 25$ μL/hr.

between model predictions and experimental results for $Wi \approx 1$ are shown in Figure 16. The velocimetry measurements for the CPyCl system reveal a Newtonian-like core surrounded by thin shear bands of fluid with high local shear rate. The linear increase in $\delta(y)$ with y in the core region is also quantitatively described by the Ellis model, confirming the validity of the stress-optical relationship for this micellar system as well as the utility of this model in predicting fully-developed channel flow of viscoelastic micellar liquids at low Wi. **We note that the centerline retardance in Figure 16 (b) is essentially zero, confirming that spatial blurring due to the finite aperture of the incident light is negligible**. Similar profiles for the shear-thinning CTAB system at $Wi = 0.7$ are shown in Figure 16. The predicted velocity profile captures the measured results in the core of the flow, and the profiles near the walls agree within experimental uncertainty. The predicted retardance profile also agrees with experimental values in the middle of the channel. The model over-predicts retardance near the walls due to the anticipated presence of normal stress there and the gradual breakdown in the stress-optical rule seen for $\dot{\gamma} > 0.5$ s^{-1} in Figure 5 (b).

The measured azimuthal angle also differs from the predicted values indicating higher than anticipated molecular alignment with the flow even at this low Wi.

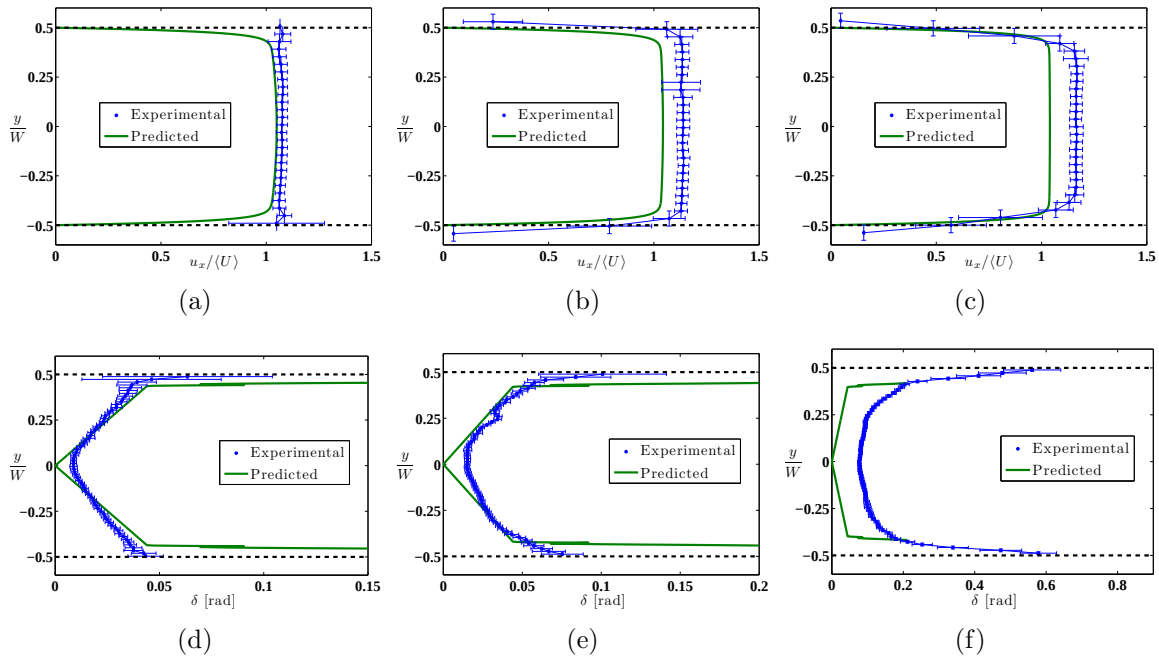

FIG. 17. Representative non-dimensionalized experimental and predicted velocity (a)-(c) and retardance (d)-(f) profiles at different Wi for the 100:60 mM CPyCl:NaSal system in the rectangular duct at $L_{obs}/D_h = 134$. (a) & (d) $Wi = 5$, $Q = 100$ μL/hr. (b) & (e) $Wi = 11$, $Q = 250$ μL/hr. (c) & (f) $Wi = 45$, $Q = 1000$ μL/hr.

Now that we have established the ability of the rheo-PIV system and the microfluidic birefringence measurements to probe quantitatively the kinematics and state of stress in a flowing complex liquid at moderate Weissenberg number, we use these techniques to explore strongly viscoelastic channel flows for larger Wi. A series of profiles for the CPyCl system at $Wi > 1$, but $De < 1$ are shown in Figure 17. The Ellis model predictions capture the general form of the experimentally-measured velocity and retardance profiles at $Wi = 5$ to within experimentally resolvable limits. The discrepancy between the model predictions and experimental results increases at high Wi. The systematic underprediction of the velocity in the plug-like core may be due to the confining effects of the upper and lower channel walls. The finite aspect ratio of the channel ($\Lambda = 7.7$) necessitates a higher effective plug velocity than the prediction of the two dimensional model. Velocimetry measurements at $5 < Wi < 100$ also indicate that three dimensional kinematic effects at the bottom of the channel are confined to less than 15% of the channel height, **as noted before from the**

numerical integration of the velocity profiles. This amount is of the same order as the underprediction shown in Figure 17 (b) and (c) (see Appendix A). Additional uncertainty can be attributed to the inability of the simple Ellis model to capture in any quantitative way the underlying shear-banding dynamics associated with the CPyCl solution as Wi is increased. Specifically, it cannot describe the evolution in the underlying microstructure that is associated with the stress degeneracy in the shear-banding regime corresponding to $Wi > 1$ and which can be observed in the viscometric measurements, shown in Figure 3.

With increasing Wi, narrow, localized regions of high retardance emerge near the walls of the channel, whose intensity increases with increasing flow rate, see also Figure 12. These retardance bands confirm the existence of shear-bands in this fluid and are at least qualitatively captured by the Ellis model. It is noteworthy that the retardance in the unbanded region of the flow near the center of the channel, where shear stress should dominate elastic stress, increases only slightly with increasing Wi, compared to the large increase in retardance in the shear-bands near the wall. This small change is well predicted by the Ellis model and is a result of the 'spurt' effect seen previously for this CPyCl system [Mair & Callaghan (1997); Méndez-Sánchez *et al.* (2003)], whereby a constant wall shear stress is associated with a many fold increase in the average velocity $\langle U \rangle$ and thus Wi. Quantitative discrepancies between the measured and predicted retardance in the banded region of flow, especially for $Wi = 45$ in Figure 17 (f), may result from a break down in the stress-optical rule. The validity of the stress-optical rule was not verified for high shear rates in the shear-banding regime, $\dot{\gamma} \sim O(10^2)$ s^{-1}, by the measurements shown in Figure 5 (a), so it is unrealistic that extrapolations with this rule well into the stress plateau will yield completely quantitative agreement with experiment.

In nearly all measurements, a finite retardance along the centerline ($y = 0$) of the channel is observed, differing from the predictions of the Ellis model for two dimensional flow. **Since a near-zero centerline retardance was observed in the CPyCl at low Wi, we believe this finite retardance is not an artifact of the finite aperture of the incident light, and it** can be attributed to several different reasons. Firstly, the measured retardance is the result of an integrated signal along the pathlength of the incident lightwave through a truly three-dimensional flow. Secondly, errors may arise from the inability of the model to predict diffusive coupling of elastic stresses from the regions of high to low shear rate shown in Figure 15 (b). Microstructural stress diffusion can lead to non-local effects

[Masselon *et al.* (2008)], that are not captured by the predictions of the simple Ellis model, and more sophisticated models, such as those discussed by [Cromer *et al.* (2010); Olmsted *et al.* (2000); Vasquez *et al.* (2007)] are needed to capture non-local effects.

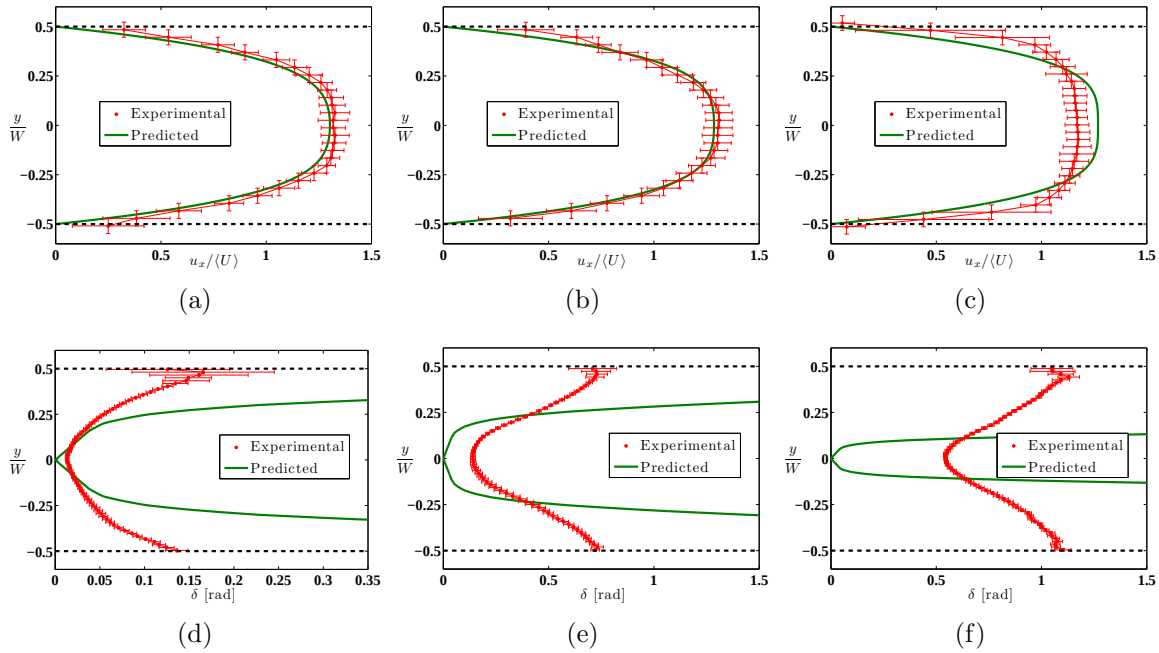

FIG. 18. Representative non-dimensionalized experimental and predicted velocity (a)-(c) and retardance (d)-(f) profiles at different Wi for the 30:240 mM CTAB:NaSal system in the rectangular duct at $L_{obs}/D_h = 134$. (a) & (d) $Wi = 3$, $Q = 100$ μL/hr. (b) & (e) $Wi = 7$, $Q = 250$ μL/hr. (c) & (f) $Wi = 67$, $Q = 2,500$ μL/hr.

Velocity and retardance profiles for the shear-thinning CTAB system at $Wi > 1$ and $De < 1$ are presented in Figure 18. In contrast to the CPyCl system, the velocimetry measurements of the CTAB solution do not reveal plug-like flow profiles even up to the maximum flow rate ($Wi = 67$) for which velocimetry measurement were made; the measured and predicted velocity profiles both indicate strong shear-thinning behavior. No regions of localized, high retardance can be identified in the birefringence measurements for the CTAB system. The Ellis model is capable of predicting only some of the features observed for the CTAB solution at these Weissenberg numbers. As Wi is increased, the agreement between the experimental and predicted velocity profiles is steadily reduced. In particular, using the model parameters listed in Table II for $Wi = 67$ the measured shear rate near the channel walls is greater than the predicted value by approximately a factor of two. This deviation from predicted behavior indicates a more dramatically reduced viscosity than that predicted

by the Ellis model at the corresponding shear rate. Estimates of the shear rate near the wall at this Wi using the Ellis model are on the order of 100 s^{-1}, which coincides roughly with the apparent stress plateau observed for this fluid in Figure 4 (b).

Deviations between experimental and predicted results for the CTAB system at high deformation rates may be attributed to the same factors given previously for the CPyCl system, including a breakdown in the stress-optical rule for $\lambda_M \dot{\gamma} \geq 1$ seen in Figure 5 (b). The measured and predicted profiles typically differ by a factor of at least two, which is approximately the extent to which the stress-optical rule fails in Figure 5. Additionally, a simple generalized Newtonian model like the Ellis model can only be expected to capture some of the gross features of the shear rheology of the CTAB system, since it cannot capture the combined shear-thinning and apparent shear-banding behavior seen in this system for $30 < \dot{\gamma} < 100$ s^{-1} in Figure 4 (b). Clearly a more sophisticated viscoelastic constitutive model is necessary to predict accurately the stress field and the resulting birefringence in complex micellar fluids for $Wi \gg 10$.

IV. CONCLUSION

The primary goal of this study has been the development and refinement of non-invasive instrumentation for quantifying the rheological response of complex fluids undergoing high rate deformations in microfluidic devices. Unique to this work is the adaptation of a commercially available birefringence microscopy system, originally designed to examine biological systems [Shribak & Oldenbourg (2003)] for optical rheometry. The greatest strengths of the ABRIO^{TM} system in probing the rheo-optical behavior of complex fluids are its ease of use and its ability to achieve highly spatially resolved measurements of the the viscometric flow of a complex fluid as it deforms in a microfluidic device.

The calibration experiments discussed here focused on the canonical case of flow in a rectilinear microchannel. We compare μ-PIV and FIB measurements of two worm-like micellar solutions against the predictions of a relatively simple constitutive model in order to demonstrate that the ABRIO^{TM} system can be reliably used for quantitative optical rheometry. The two test fluids, one a shear-banding 100:60 mM CPyCl:NaSal system, and the other a shear-thinning 30:240 mM CTAB:NaSal system, were first characterized using conventional macroscale as well as microscale rheometric techniques in order to determine the viscomet-

ric material functions that can then be used to predict their flow characteristics in more complex microfluidic geometries.

At the low to moderate Weissenberg and Deborah numbers ($Wi < 10$, $De < 1$) for which use of a generalized Newtonian fluid model is anticipated to be most accurate, we find near-quantitative agreement between the predictions of the model and experimental measurements of the flow kinematics as well as the retardance measured with the birefringence microscopy instrument. This agreement validates the use of the ABRIO system for quantitative optical microrheometry. At high Weissenberg numbers, the μ-PIV and FIB results indicate that the material response of the fluids is more complex than can be predicted by such a simple generalized Newtonian fluid constitutive model. In the future, full 2D numerical computations with suitable viscoelastic constitutive equations that describe the microstructural evolution in the fluids can be compared with this complete data set. Having demonstrated the ability of this coupled μ-PIV/birefringence microscopy system for studying a simple rectilinear channel flow, we can confidently utilize it for making FIB measurements in considerably more complex microfluidic flows with mixed shearing/extensional kinematics, which will be the subject of future work.

ACKNOWLEDGMENTS

The authors wish to acknowledge Dr. Michael Shribak for helpful discussions and insight into the use of the ABRIO System. We are also especially indebted to Dr. Matthew Helgeson and Dr. Norman Wagner for granting us use of their optical rheometry system to measure the stress-optical coefficients of both test fluids. Finally, Marc-Antoine Fardin has been especially helpful in this study and a source of many fruitful discussions.

Appendix A: Three dimensional and high Weissenberg number effects

In the previous sections, comparisons between experimental results and the predictions of the Ellis model were made only for dimensionless shear rates corresponding to spatially fully-developed flow, $De \leq 1$. For these conditions, comparison with the steady state solution of a non-Newtonian constitutive model was appropriate. By contrast, as the flow rate is increased and the residence time in the channel decreases (corresponding to $De > 1$), the

flow becomes increasingly unsteady in the Lagrangian frame and the viscoelastic stresses may not be fully-developed at a particular observation point, L_{obs}.

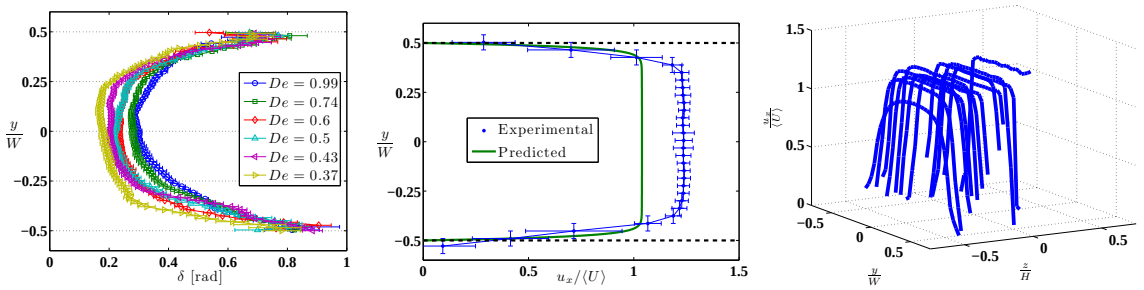

(a) (b) (c)

FIG. A1. 100:60 mM CPyCl:NaSal. $Wi = 113$, $Re_0 = 1.4 \times 10^{-5}$, $Q = 2,500$ μL/hr. (a) Uncorrected retardance profiles at different De (different L_{obs}) in the rectangular duct. (b) Representative experimental and predicted velocity profiles for $De = 0.43$, ($L_{obs} = 3.5$ cm, $z/H = 0.25$). (c) Non-dimensionalized experimental velocity profiles taken at $50 \leq z \leq 900$ μm above the bottom of the channel for $De = 0.43$, ($L_{obs} = 3.5$ cm).

To explore this continuing spatial development in the flow, we use the birefringence microscope system to plot and compare lateral profiles in the retardance at different axial positions along the channel. This spatial development in the flow can be noticed, in particular, in the pseudocolor plot for the flowing CTAB solution at $Wi = 266$ in Figure 14. At any selected y-position, the birefringence intensity increases in the direction of flow even over the short distance $\Delta x_{im} = 700$ μm of channel length that is in view in a single microscope image. Furthermore, the magnitude of the peak retardance across the width of the channel *decreases* with increasing flow rate for $Wi \geq 133$ in the CTAB system and $Wi \geq 454$ in the CPyCl system. These results suggest that at high flow rates, the residence time for material elements in the channel is insufficient for the local viscoelastic stresses to develop fully.

The evolving retardance profile for the CPyCl fluid at $Wi = 113$ is captured by the spatially averaged profiles shown in Figure A1 (a). With decreasing Deborah number ($De \equiv \lambda_M \langle U \rangle / L_{obs}$), corresponding to observation distances further along the channel, the retardance near the middle of the channel ($-0.25 \leq y/W \leq 0.25$) relaxes steadily as the flow approaches the fully-developed limit, $De \to 0$. For this reason, comparisons between the steady state predictions of Ellis model and the measured birefringence profiles in Section III D were restricted to measurements corresponding to $De \leq 0.25$.

The variation in $u_x(y)$ and $u_x(y, z)$ for the CPyCl system at $Wi = 113$ are also presented

in Figure A1 (b) and (c), respectively. At this flow rate, the axial velocity of the plug-like core, measured at $z/H = 0.25$, is roughly 20% greater than $\langle U \rangle$. This core velocity is greater than the axial velocity for the 1D profile predicted by the Ellis model, in part, because the model does not include a finite high shear rate viscosity, so it under predicts the thickness of the high shear rate regions in the velocity profile which give rise to the higher core velocity seen experimentally. The higher core velocity is also caused by the finite aspect ratio of the channel ($\Lambda = 7.7$) giving rise to the vertical variations in the velocity profile shown in Figure A1 (c). The variations are confined to less than 100 μm above the bottom of the channel. The Reynolds number for this flow rate is sufficiently small ($Re_0 = 1.4 \times 10^{-5}$) that the estimated entrance length for the flow kinematics is much shorter than the observation positions, (*i.e.* $L_e \ll L_{obs}$), as given by the correlation in Section III A. Therefore, the kinematics remain steady and close to two dimensional in character, as expected for low Reynolds number flow, and the evolution in the birefringence profiles observed at high Wi and De can be attributed to relaxation in the viscoelastic stress field downstream of the abrupt entrance to the flow channel.

REFERENCES

Anderson, V.J., Pearson, J.R.A., & Boek, E. S. 2006. The rheology of worm-like micellar fluids. *Rheology Reviews, The British Society of Rheology.* D.M. Binding and K. Walters (Eds.).

Berret, J.-F. 2006. Rheology of Wormlike Micelles: Equilibrium Properties and Shear Banding Transitions. *Pages 667–720 of:* Weiss, R. G., & Terech, P. (eds), *Molecular Gels.* Springer Netherlands.

Bird, R. B., Armstrong, R. C., & Hassager, O. 1987. *Dynamics of Polymeric Liquids.* 2nd edn. Vol. 1. New York, NY: John Wiley & Sons, Inc.

Cates, M. E., & Fielding, S. M. 2006. Rheology of Giant Micelles. *Advances in Physics*, **55**(7-8), 799–879.

Cromer, M., Cook, L. P., & McKinley, G.H. 2010. Pressure-driven flow of wormlike micellar solutions in rectilinear microchannels. *Journal of Non-Newtonian Fluid Mechanics.* In Press, Corrected Proof, 0377-0257.

Dealy, J.M. 2010. Weissenberg and Deborah Numbers - Their Definition and Use. *Rheology*

Bulletin (Society of Rheology), **79**(2), 14–18.

Decruppe, J. P., Cappelaere, E., & Cressely, R. 1997. Optical and rheological properties of a semi-diluted equimolar solution of cetyltrimethylammonium bromide and potassium bromide. *Journal De Physique II*, **7**(2), 257–270.

Decruppe, J. P., & Ponton, A. 2003. Flow birefringence, stress optical rule and rheology of four micellar solutions with the same low shear viscosity. *European Physical Journal E*, **10**(3), 201–207.

Degré, G., Joseph, P., Tabeling, P., Lerouge, S., Cloitre, M., & Ajdari, A. 2006. Rheology of complex fluids by particle image velocimetry in microchannels. *Applied Physics Letters*, **89**(2), 024104.

Durst, F., Ray, S., Unsal, B. & Bayoumi, O. A. 2005. The development lengths of laminar pipe and channel flows. *Journal of Fluids Engineering*, **127**(6), 1154–1160.

Fardin, M. A., Lasne, B., Cardoso, O., Grégoire, G., Argentina, M., Decruppe, J. P., & Lerouge, S. 2009. Taylor-like vortices in shear-banding flow of giant micelles. *Physical Review Letters*, **103**(2), 028302.

Feindel, K. W., & Callaghan, P. T. 2010. Anomalous shear banding: multidimensional dynamics under fluctuating slip conditions. *Rheologica Acta*, **49**(10), 1003–1013.

Fielding, S. M. 2007. Complex dynamics of shear banded flows. *Soft Matter*, **3**(10), 1262–1279.

Fischer, E., & Callaghan, P. T. 2000. Is a birefringence band a shear band? *Europhysics Letters*, **50**(6), 803–809.

Fischer, E., & Callaghan, P. T. 2001. Shear banding and the isotropic-to-nematic transition in wormlike micelles. *Physical Review E*, **64**(1), 011501.

Fuller, G. G. 1990. Optical Rheometry. *Annual Review of Fluid Mechanics*, **22**, 387–417.

Fuller, G. G. 1995. *Optical Rheometry of Complex Fluids*. Oxford University Press.

Guillot, P., Panizza, P., Salmon, J. B., Joanicot, M., Colin, A., Bruneau, C. H., & Colin, T. 2006. Viscosimeter on a microfluidic chip. *Langmuir*, **22**(14), 6438–6445.

Helgeson, M. E., Reichert, M. D., Hu, Y. T., & Wagner, N. J. 2009a. Relating shear banding, structure, and phase behavior in wormlike micellar solutions. *Soft Matter*, **5**(20), 3858–3869.

Helgeson, M. E., Vasquez, P. A., Kaler, E. W., & Wagner, N. J. 2009b. Rheology and spatially resolved structure of cetyltrimethylammonium bromide wormlike micelles through

the shear banding transition. *Journal of Rheology*, **53**(3), 727–756.

Hu, Y. T., & Lips, A. 2005. Kinetics and mechanism of shear banding in an entangled micellar solution. *Journal of Rheology*, **49**(5), 1001–1027.

Hu, Y. T., Palla, C., & Lips, A. 2008. Comparison between shear banding and shear thinning in entangled micellar solutions. *Journal of Rheology*, **52**(2), 379–400.

Humbert, C., & Decruppe, J. P. 1998. Stress optical coefficient of viscoelastic solutions of cetyltrimethylammonium bromide and potassium bromide. *Colloid and Polymer Science*, **276**(2), 160–168.

Israelachvili, J. 2007. *Intermolecular & Surface Forces*. 2nd edn. Academic Press.

Johnson, M., & Segalman, D. 1977. A model for viscoelastic fluid behavior which allows non-affine deformation. *Journal of Non-Newtonian Fluid Mechanics*, **2**, 255–270.

Kang, K., Lee, L. J., & Koelling, K. W. 2005. High shear microfluidics and its application in rheological measurement. *Experiments in Fluids*, **38**(2), 222–232.

Kang, K., Koelling, K. W., & Lee, L. J. 2006. Microdevice end pressure evaluations with Bagley correction. *Microfluidics and Nanofluidics*, **2**(3), 223–235.

Kefi, S., Lee, J., Pope, T. L., Sullivan, P., Nelson, E., *et al.* 2005. Expanding Applications of Viscoelastic Surfactant Solutions. *Oilfield Review*, **Winter 2004/2005**, 10–23.

Larson, R. G. 1998. *The Structure and Rheology of Complex Fluids*. Oxford University Press.

Lee, J. Y., Fuller, G. G., Hudson, N. E., & Yuan, X. F. 2005. Investigation of shear-banding structure in wormlike micellar solution by point-wise flow-induced birefringence measurements. *Journal of Rheology*, **49**(2), 537–550.

Lerouge, S., Decruppe, J. P., & Berret, J.-F. 2000. Correlations between rheological and optical properties of a micellar solution under shear banding flow. *Langmuir*, **16**(16), 6464–6474.

Lerouge, S., Decruppe, J. P., & Olmsted, P. D. 2004. Birefringence banding in a micellar solution or the complexity of heterogeneous flows. *Langmuir*, **20**(26), 11355–11365.

Lerouge, S., Fardin, M. A., Argentina, M., Grégoire, G., & Cardoso, O. 2008. Interface dynamics in shear-banding flow of giant micelles. *Soft Matter*, **4**(9), 1808–1819.

Lerouge, S., & Berret, J.-F. 2010. *Shear-Induced Transitions and Instabilities in Surfactant Wormlike Micelles*. Advances in Polymer Science. Springer Berlin/Heidelberg.

Li, J. M., & Burghardt, W. R. 1995. Flow Birefringence in Axisymmetrical Geometries.

Journal of Rheology, **39**(4), 743–766.

Lu, C.-Y. D., Olmsted, P. D., & Ball, R. C. 2000. Effects of nonlocal stress on the determination of shear banding flow. *Physical Review Letters*, **84**(4), 642–645.

Mair, R. W., & Callaghan, P. T. 1997. Shear flow of wormlike micelles in pipe and cylindrical Couette geometries as studied by nuclear magnetic resonance microscopy. *Journal of Rheology*, **41**(4), 901–924.

Masselon, C., Salmon, J. B., & Colin, A. 2008. Nonlocal effects in flows of wormlike micellar solutions. *Physical Review Letters*, **100**(3), 038301.

McLeish, T. C. B., & Ball, R. C. 1986. A molecular approach to the spurt effect in polymer melt flow. *Journal of Polymer Science Part B-Polymer Physics*, **24**(8), 1735–1745.

Meinhart, C. D., Wereley, S. T., & Gray, M. H. B. 2000. Volume illumination for two-dimensional particle image velocimetry. *Measurement Science & Technology*, **11**(6), 809–814.

Méndez-Sánchez, A.F., Pérez-González, J., de Vargas, L., Castrejón-Pita, J.R., Castrejón-Pita, A.A., & Huelsz, G. 2003. Particle image velocimetry of the unstable capillary flow of a micellar solution. *Journal of Rheology*, **47**(6), 1455–1466.

Miller, E., & Rothstein, J. P. 2007. Transient evolution of shear-banding wormlike micellar solutions. *Journal of Non-Newtonian Fluid Mechanics*, **143**(1), 22–37.

Nghe, P., Degré, G., Tabeling, P., & Ajdari, A. 2008. High shear rheology of shear banding fluids in microchannels. *Applied Physics Letters*, **93**(20), 204102.

Nghe, P., Fielding, S. M., Tabeling, P., & Ajdari, A. 2010. Interfacially driven instability in the microchannel flow of a shear-banding fluid. *Physical Review Letters*, **104**(24), 248303.

Oliveira, M. S. N., Rodd, L. E., McKinley, G. H., & Alves, M. A. 2008. Simulations of extensional flow in microrheometric devices. *Microfluidics and Nanofluidics*, **5**(6), 809–826.

Olmsted, P. D., Radulescu, O., & Lu, C. Y. D. 2000. Johnson-Segalman model with a diffusion term in cylindrical Couette flow. *Journal of Rheology*, **44**(2), 257–275.

Olmsted, P. D. 2008. Perspectives on shear banding in complex fluids. *Rheologica Acta*, **47**(3), 283–300.

Pathak, J. A., & Hudson, S. D. 2006. Rheo-optics of equilibrium polymer solutions: Wormlike micelles in elongational flow in a microfluidic cross-slot. *Macromolecules*, **39**(25), 8782–8792.

Pipe, C. J., Majmudar, T. S., & McKinley, G. H. 2008. High shear rate viscometry. *Rheologica Acta*, **47**(5-6), 621–642.

Pipe, C. J., & McKinley, G. H. 2009. Microfluidic rheometry. *Mechanics Research Communications*, **36**(1), 110–120.

Poole, R. J. and Ridley, B. S. 2007. Development-length requirements for fully developed Laminar pipe flow of inelastic non-Newtonian liquids. *Journal of Fluids Engineering*, **129**(10), 1281–1287.

Raffel, M., Willert, C., & Kompenhans, J. 1998. *Particle Image Velocimetry*. Springer-Verlag.

Raudsepp, A., & Callaghan, P. T. 2008. A rheo-optical study of shear rate and optical anisotropy in wormlike micelles solutions. *Soft Matter*, **4**(4), 784–796.

Rehage, H., & Hoffmann, H. 1991. Viscoelastic surfactant solutions - model systems for rheological research. *Molecular Physics*, **74**(5), 933–973.

Renardy, Y. Y. 1995. Spurt and instability in a two-layer Johnson-Segalman liquid. *Theoretical and Computational Fluid Dynamics*, **7**(6), 463–475.

Rodd, L. E., Scott, T. P., Boger, D. V., Cooper-White, J. J., & McKinley, G. H. 2005. The inertio-elastic planar entry flow of low-viscosity elastic fluids in micro-fabricated geometries. *Journal of Non-Newtonian Fluid Mechanics*, **129**(1), 1–22.

Rothstein, J. P. 2008. Strong flows of viscoelastic wormlike micelle solutions. *Rheology Reviews, The British Soceity of Rheology*, 1–43. D.M. Binding and K. Walters (Eds.).

Salmon, J. B., Colin, A., & Manneville, S. 2003. Velocity profiles in shear-banding wormlike micelles. *Physical Review Letters*, **90**(22), 228303.

Shikata, T., Dahman, S. J., & Pearson, D. S. 1994. Rheooptical Behavior of Wormlike Micelles. *Langmuir*, **10**(10), 3470–3476.

Shribak, M., & Oldenbourg, R. 2003. Techniques for fast and sensitive measurements of two-dimensional birefringence distributions. *Applied Optics*, **42**(16), 3009–3017.

Soulages, J., Oliveira, M. S. N., Sousa, P. C., Alves, M. A., & McKinley, G. H. 2009. Investigating the stability of viscoelastic stagnation flows in T-shaped microchannels. *Journal of Non-Newtonian Fluid Mechanics*, **163**(1-3), 9–24.

Takahashi, T., Shirakashi, M., Miyamoto, K., & Fuller, G. G. 2002. Development of a double-beam rheo-optical analyzer for full tensor measurement of optical anisotropy in complex fluid flow. *Rheologica Acta*, **41**(5), 448–455.

Tanner, R. I., & Keentok, M. 1983. Shear fracture in cone–plate rheometry. *Journal of Rheology*, **27**(1), 47–57.

Turner, M. S., & Cates, M. E. 1991. Linear viscoelasticity of living polymers - a quantitative probe of chemical relaxation-times. *Langmuir*, **7**(8), 1590–1594.

Vasquez, P. A., McKinley, G. H., & Cook, L. P. 2007. A network scission model for wormlike micellar solutions - I. Model formulation and viscometric flow predictions. *Journal of Non-Newtonian Fluid Mechanics*, **144**(2-3), 122–139.

Wheeler, E. K., Fischer, P., & Fuller, G. G. 1998. Time-periodic flow induced structures and instabilities in a viscoelastic surfactant solution. *Journal of Non-Newtonian Fluid Mechanics*, **75**(2-3), 193–208.

Wunderlich, I., Hoffmann, H., & Rehage, H. 1987. Flow birefringence and rheological measurements on shear induced micellar structures. *Rheologica Acta*, **26**(6), 532–542.

Yamamoto, T., Hashimoto, T., & Yamashita, A. 2008. Flow analysis for wormlike micellar solutions in an axisymmetric capillary channel. *Rheologica Acta*, **47**(9), 963–974.

Zhou, L., Vasquez, P. A., Cook, L. P., & McKinley, G. H. 2008. Modeling the inhomogeneous response and formation of shear bands in steady and transient flows of entangled liquids. *Journal of Rheology*, **52**(2), 591–623.